Morphology and Three-Dimensional Inhalation Flow in Human Airways in Healthy and Diseased Subjects

A Thesis
SUBMITTED TO THE FACULTY OF
UNIVERSITY OF MINNESOTA
BY

Tristan Van de Moortele

IN PARTIAL FULFILLMENT OF THE REQUIREMENTS
FOR THE DEGREE OF
MASTER OF SCIENCE

Filippo Coletti, Adviser

September 2017

Acknowledgements

Foremost, I would like to thank Professor Coletti for not only the opportunity to work in his fantastic research lab, but for his constant teaching, advice, and guidance. This research project has been immensely rewarding and the most enjoyable part of my tenure as both an undergraduate and graduate student at the University of Minnesota. Additionally, I would like to thank the two fantastic post-docs I worked with, Andras Nemes and Omid Amili, for their never-ending technical support and help performing experiments. At the Center for Magnetic Resonance Research, Sebastian Schmitter and Ute Georke were a tremendous help teaching us how to use the MRI technology and for their MRI sequence writing. Lastly, I thank my lab mates Kyle Winters, Sahar Jalal, and Yan Ming Tan for their help in experiments and data analysis, but more importantly for their unwavering friendship.

Abstract

We investigate experimentally the relation between anatomical structure and respiratory function in healthy and diseased airways. Computed Tomography (CT) scans of human lungs are analyzed from the data base of a large multi-institution clinical study on Chronic Obstructive Pulmonary Disease (COPD). Through segmentation, the 3D volumes of the airways are determined at total lung capacity. A geometric analysis provides data on the morphometry of the airways, including the length and diameter of branches, the child-to-parent diameter ratio, and branching angles. While several geometric parameters are confirmed to match past studies for healthy subjects, previously unreported trends are reported on the length of branches. Specifically, in most dichotomous airway bifurcation, the branch of smaller diameter tends to be significantly longer than the one of larger diameter. Additionally, the branch diameter tends to be smaller in diseased airways than in healthy airways up to the 7th generation of bronchial branching. 3D fractal analysis is also performed on the airway volume. Fractal dimensions of 1.89 and 1.83 are found for healthy non-smokers and declining COPD subjects, respectively, furthering the belief that COPD (and lung disease in general) significantly affects the morphometry of the airways already in early stages of the disease. To investigate the inspiratory flow, 3D flow models of the airways are generated using Computer Aided Design (CAD) software and 3D printed. Using Magnetic Resonance Velocimetry (MRV), 3-component 3D flow fields are acquired for steady inhalation at Reynolds number Re ~ 2000 defined at the trachea. Analysis of the flow data reveals that diseased subjects may experience greater secondary flow strength in their conducting airways, especially in deeper generations.

Table of Contents

List of Tables

List of Figures

Chapter 1: Introduction

1.1 Motivation

Chronic Obstructive Pulmonary Disease (COPD) is a lung disease typically caused by heavy smoking, or other sources of long-term exposure to harmful particles such as dense pollution. COPD can present itself as emphysema (destruction of lung tissue) or chronic bronchitis (inflammation of the bronchial tubes) which results in severe obstruction of airflow through the lungs. The deterioration of quality of life for a subject with COPD is very significant, highlighted by shortness of breath, chest tightness, chronic coughing, and in many cases exacerbation episodes that may last multiple days. If left unattended, this can lead to chronic hypoxemic respiratory failure and death COPD affects 14 million Americans, and is the United States' third leading cause of death, killing more than 100 thousand people a year (Minino et al. 2010). Unlike other leading causes of death, it is the only one that is increasing in prevalence. Although it is known that smoking is the primary risk factor for this disease, it remains unknown why only 15-20% of smokers develop COPD (Fletcher & Peto 1977). Other factors such as genetics play an important role in the progression of COPD.

Identification of biomarkers that single out subjects at risk of developing COPD would be of great importance to the creation and implementation of prevention strategies and therapies. Currently, COPD is diagnosed and characterized by completely irreversible airflow obstruction or lung function (Celli et al. 2004). This is measured by the ratio of the Forced Expiratory Volume in 1 second (FEV1) to the Forced Vital Capacity (FVC) (Rabe et al. 2007). FEV1 is the maximum volume of air a subject can exhale in 1 second after maximum inhalation, and FVC is the total volume of air a subject can exhale after maximum inhalation. A low FEV1/FVC ratio (typically cutoff at > 0.7) combined with an FEV1 that is less than 80% of what is predicted for a certain demographic are used as the diagnostic tools for COPD. While these measures are accurate predictors of disease, they do not accurately predict symptoms or symptom

severity (Antonelli-Incalzi et al. 2003). Additionally, there is little understanding of the early phases of COPD, in the stages before diagnosis is currently possible.

In the study of any airway disease, specifically when geared towards the identification of biomarkers, it is useful to consider the structure-function relationship of the airways. The "structure" refers to the geometry and morphological features of the airways, while the "function" refers to the airflow through the airways including particle transport and gas mixing. The geometric properties of the bronchi influence the physiology of the airways, which also affect airflow resistance. Changes in those features directly impact the function of the lungs, i.e. altering gas mixing as well as transport and deposition of particles. Therefore, the inhalation of both harmful and therapeutic particles may provoke a different physiological response depending on the airway structure. By studying the structure and the function of the airways, individually and in their mutual relation, we can start to gain an understanding of the role of respiratory fluid mechanics in COPD.

1.2 Previous work

1.2.1 Morphology of the airways

Classic morphometric studies, such as Weibel's symmetric model and Horsfield's asymmetric model of the airways (Weibel 1963 and Horsfield et al. 1971), laid the foundation for morphological analysis of the airways. These models represent the airways as a self-similar structure of dichotomously bifurcating tubes. The geometrical parameters governing these models were calculated from a single excised lung each and various measurements of geometry were done by hand. For example, Weibel found that the child-to-parent branch diameter ratio (also referred to as the homothety ratio) was approximately h = 2^(-1/3). Other geometric parameters, such as length-to-diameter ratio and sibling diameter ratio, have been explored in many studies, using both excised lungs and in vivo scans (using Magnetic Resonance Imaging, MRI, and Computed Tomography, CT) (Horsfield 1971, Phillips et al. 1995, Sapoval et al. 2002, Tawhai et al.

2004, Weibel 1963). These studies corroborate the idea of a self-similar structure purported by the classic models of Weibel and Horsfield, for they find that the geometric parameters have similar values throughout all airways. The nature of this self-similar structure is thought to be related to the lung function. The aforementioned child-to-parent diameter ratio is nearly optimal to minimize air flow resistance during normal breathing patterns (Murray 1926, West et al. 1997, and Wilson 1969). Other studies have looked at the self-similarity of the airways through its fractal dimension (Glenny et al. 2011, Goldberger et al. 1991, Mandelbrot 1983, Mandelbrot 1990, Weibel 2009). For a large portion of scales related to the airways, the airway tree has been shown to have a consistent fractal architecture – i.e., having a well-defined Hausdorff dimension (Hausdorff 1918). This can be determined through box-counting, either in 3-D or 2-D projections. This type of fractal analysis is common in many biological settings, such as the vascular tree in the retina and the splitting of fern leaves (Masters 2004, Campbell 1994).

1.2.2 Fluid mechanics analysis of the airways

As pointed out in recent reviews (Grotberg 1994; Kleinsteuer & Zhang 2010) the range of flow phenomena that occurs simultaneously during respiration is broad, including laminar-to-turbulent transition, separation and recirculation, dispersed phase transport and deposition, and fluid-structure interaction. Devising in vitro (i.e., experimental) or in silico (i.e., computational) models that account for all aspects is presently not realistic, various levels of idealization have been accepted. Previous studies concerning the fluid mechanics of the airways have often explored Weibel's simplified airway model, through Particle Imaging Velocimetry (PIV) as well as Computational Fluid Dynamics (CFD). While many key breathing mechanics are thought to be captured by this model (see reviews by Pedley 1977 and Grotberg 1994, as well as Jalal et al. 2016), the ability to study subject specific geometries is of great interest, for little is known about the true behavior of airflow in the airways. De Backer et al. (2008, 2010), Choi et al. (2010) have applied CFD to subject specific models aimed at exploring

inhalation and exhalation flow throughout the upper airways. PIV has allowed for 2D flow field analysis, but recent studies using Magnetic Resonance Velocimetry (MRV) have explored the 3D flow fields of the upper airways. Banko et al. (2015, 2016) successfully created a subject-specific model of the airways and reconstructed the 3D flow field using MRV.

1.3 Objectives

The present work aims to explore both the structure and the function of the human airways in healthy and diseased subjects. Comparisons between COPD and healthy subjects will be made with the goal of achieving a better understanding of COPD pathophysiology, which could lead to better treatment, diagnosis, and prevention methods. The structure of the airways is analyzed through a geometric analysis of the airway tree in the first few (typically seven) generations of bronchial branching. CT scans obtained from a large clinical study are reconstructed into 3D volumes, from which various geometrical parameters are evaluated. Using MRI technology, 3D flow fields of inhalation are acquired during in vitro experiments. The analysis of these 3D flow fields provide insight into the function of the human airways. Through these two analyses, differences in structure and function between healthy and diseased airways lead to new insights regarding COPD in particular, and respiration physiology in general.

Chapter 2: Experimental Methods

2.1 Morphological analysis

2.1.1 Subject selection

This study was approved by the University of Minnesota Institutional Review Board (IRB# 1410E54644). Subjects are selected from the database assembled by the COPDGene project (Reagan et al. 2011), a large longitudinal study which carried out lung function tests and computed tomography (CT) scans. This data was obtained both at the first subject visit (baseline) and at a second visit 5 years later. For this study, four groups of subjects were selected for comparison as listed below.

- *Decliner COPD*: subjects who had lung function limitation at the baseline visit (FEV1/FVC < 0.7 and FEV1 larger than 80% of the value predicted), and at the five-year visit showed large FEV1 decline (< 0.5 liters).

- *Stable COPD*: subjects with similar limitation at baseline as the Decliner COPD group, but minimal to no FEV1 decline after five years.

- *Normal smoker*: subjects with healthy FEV1 both at the baseline and five-year visit.

- *Normal non-smoker*: non-smoking subjects with healthy FEV1 both at the baseline and five-year visit.

The three groups of smokers (decliner COPD, stable COPD, and normal smoker) are comprised of 18 subjects each, while the normal non-smoker group is comprised of 36 subjects. All subjects are of similar age range and gender was split evenly between male

and female for each group (except the normal non-smoker group which has a 10 and 26 subject split for males and females, respectively).

2.1.2 CT scan segmentation

The CT scans from the COPDGene study were acquired using multidetector computed tomography (MDCT). The scan resolution ranged from 0.5 mm to 0.75 mm in slice thickness. When reconstructed in 3D, the average voxel size was 0.3 mm^3, and was nearly isotropic. For all subjects, scans were obtained at both the maximal lung inflation and at passive expiration points of the breathing cycle.

Using the software Mimics (Materialise, Leuven, Belgium), CT scans (baseline inhalation and exhalation, as well as 5-year inhalation and exhalation for the decliner COPD group) of all selected subjects were segmented into two sets of 3D reconstructions. First, the bronchial airway volume was reconstructed for the morphometric analysis using the maximal lung inflation scan. We choose to reconstruct the maximal inflation scan because, while the geometry of the airways fluctuates with the breathing cycle, deposition of particles in the airways (including harmful particles that lead to COPD) primarily occurs during peak inhalation. Airways were reconstructed as deep as the resolution of the scans allowed, typically between the 5^{th} and 10^{th} generation, depending on the scan as well as spatial location and orientation. This volume was then processed using a smoothing algorithm to remove spurious edges that appear due to limited spatial resolution. Following this, the terminal branches were trimmed such that their cross-section is normal to the branch path. The centerline is then determined and extracted by the software through a semi-automatic process. This also returns information at each point in the centerline including spatial location, branch diameter, branch aspect ratio, branch curvature, and local centerline direction. Secondly, the total air volume of each of the lung's five lobes – right upper lobe (RUL), right middle lobe (RML), right lower lobe (RLL), left upper lobe (LUL), and left lower lobe (LLL) – is determined for both the maximal lung inflation and passive exhalation scans to analyze the lobar ventilation. These volumes are also smoothed using the Mimics smoothing algorithm. All

reconstructed volumes are converted to stereolithography (STL) files for further analysis. STL files discretize a 3D object into a triangulated surface. The lung anatomy analysis process is summarized in Figure 1.

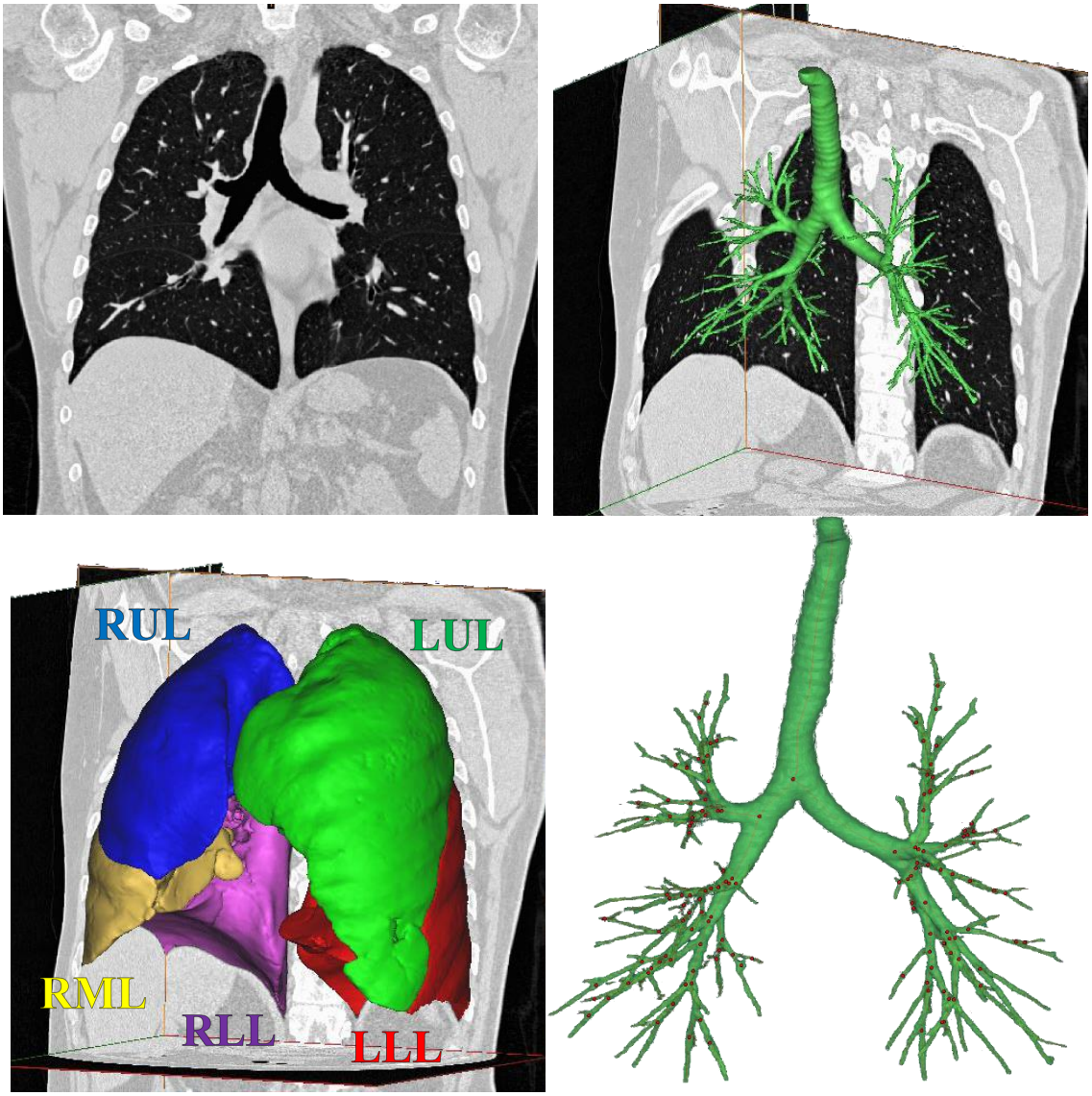

Fig. 1 Segmentation process of CT images. Upper left: slice of a CT scan. Upper right: segmented airway tree volume. Lower Left: segmented lobar volumes. Lower right: segmented airway tree volume overlapped with the extracted centerline and branching points.

2.1.3 Geometrical parameters, fractal analysis, lobar ventilation

Once the centerline of the airway volume is obtained, it is processed through an algorithm that identifies the trachea and orders the branches according Weibel's generational ordering of branches. In this ordering system, the trachea corresponds to the zero-th generation G0 and each subsequent bifurcating branch is one order higher. This work examines the geometrical properties of the airways for all branches until G7 (i.e., all branches within 7 consecutive bifurcations from the trachea). The more distal the airway, the smaller the diameter, according to the child-to-parent diameter ratio (Weibel 1963). Therefore, the fixed scan resolution will fail to reconstruct more and more branches in higher generations. This is shown in Figure 2, which plots the average number of branches for each subject vs. the generation number. This is overlaid with a plot of 2^N (N being generation number), which is the expected number of branches at each generation. Up to G5, almost every branch is recovered, while G6 and G7 show significant drop-off due to airways becoming too small to be fully captured by the CT scan. Instances of trifurcations occur regularly between G3 and G5, leading to more branches recovered than expected in those generations.

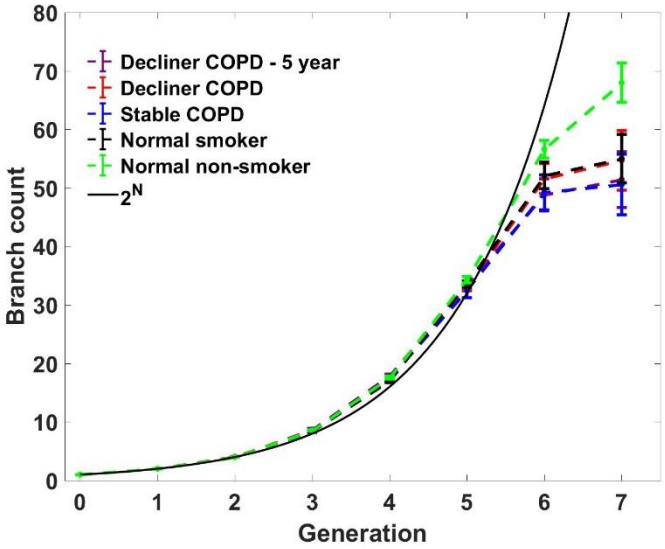

Fig. 2 Branch count of airways vs. generation, averaged over all cases in each subject group. The black solid line represents the ideal number of branches in a perfect dichotomously branching airway tree. Error bars reported in standard error.

Once the centerline of all airways has been identified, the algorithm calculates a various geometrical parameters and angles that characterize the morphology of the airways. Table 1 provides a list and description of these parameters, which are determined at every branch/bifurcation location. These are analyzed both from a global (first seven generations) and generational viewpoint. When analyzing sibling branches, the major/minor child is defined to be the one of larger/smaller diameter.

Parameter	**Description**
D (mm)	Diameter of a branch, we define D_0 as the trachea diameter
L (mm)	Length of a branch, typically reported as the ratio L/D_0
L/D	Ratio of the length to diameter of a branch
$(L/D)_{min}$	Ratio of the length to diameter of the minor branch of sibling branches
$(L/D)_{maj}$	Ratio of the length to diameter of the major branch of sibling branches
L_{min}/L_{maj}	Ratio of the lengths of the minor to major branch of sibling branches
h	Ratio of the diameters of a child branch to its parent branch
h_{min}	Ratio of the diameters of the minor child branch to its parent branch
h_{maj}	Ratio of the diameters of the major child branch to its parent branch
m	Exponent satisfying the relation of: $D_{parent}^{m} = D_{min}^{m} + D_{maj}^{m}$
D_{min}/D_{maj}	Ratio of the diameters of a minor child branch to the major child branch
θ_{min} [°]	Branching angle of the minor child branch to its parent
θ_{maj} [°]	Branching angle of the major child branch to its parent
θ [°]	Branching angle between two child branches. It is the sum of the minor and major branching angles.
$\lvert\theta_{min} - \theta_{maj}\rvert/\theta$	Ratio of the difference in branching angles to the total branching angle
ϕ [°]	Rotation angle of a pair of child branches to the parent and parent's sibling branches. It is the angle between the plane made by these two pairs of siblings.
δ [°]	Inclination angle of a pair of child branches to the parent branch. It is the angle between the plane made by the two child branches and the axis of the parent branch.

Table 1 List of the various geometrical parameters analyzed for each subject using the extracted centerline information.

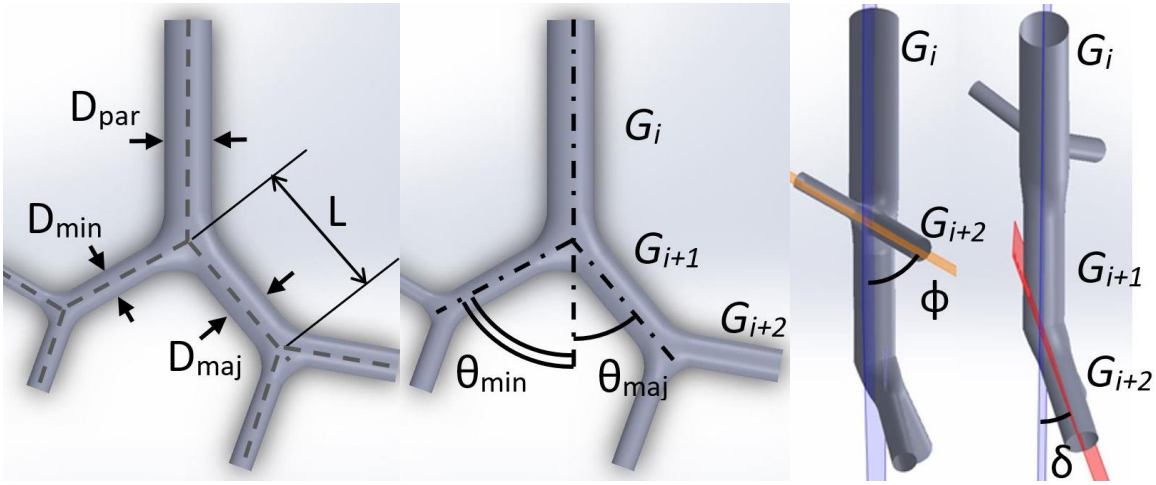

Fig. 3 Illustrations of the various geometrical parameters analyzed. Left: branch dimensions. Middle: generational ordering and branching angle. Right: generational ordering, rotation angle, and inclination angle.

Figure 3 provides a schematic view of the base parameters from which all other parameters can be determined. The right panel illustrates the branch dimensions, D and L. labeling the minor and major diameter we show how siblings are classified as such. In the middle panel, the generational ordering system (Weibel method) is shown. The generation of a branch is one more than its parent. Also shown is the minor and major branching angles θ_{min} and θ_{maj}, which are determined from the axes of the child branches and the axis of the parent branch. The left panel of Figure 3 shows the two other angles of interest, the rotation angle ϕ and the inclination angle δ. These are determined using the plane made by the axes of the two child branches and the plane made by the axes of the parent branch and its sibling branch.

The 1963 Weibel model of the airways previously mentioned is symmetric and dichotomous (i.e., every parent branch has exactly two child branches) at every branching point. The child-to-parent diameter ratio h is constant through all the branches, and all sibling branches have equal diameters ($D_{min}/D_{maj} = 1$). The length over diameter ratio L/D and the branching angle θ are also constant for all branches. The rotation angle ϕ and inclination angle δ are zero. Differences between this idealized model and real subject-

specific geometries are of great importance in order to quantify the shortcomings and inaccuracies ideal models have.

The parameters above describe the exact geometric way the airways bifurcate throughout the generations. However, they may not be the best way to characterize the self-similarity of the airways. With the STL file of the airway volume, the fractal nature (or lack thereof) of the airway tree can be explored. Superimposing the STL onto a binary cubic matrix of size 625 by 625 by 625, and the box-counting dimension is calculated. This is done by starting with a box size of 1 voxel and counting the number of boxes needed to fully cover every voxel in the cubic matrix which contains part of the STL. This process is repeated, each time doubling the box size (i.e. second iteration would have a box size of 2 voxels, third iteration would have a box size of 4 voxels, etc.) until the box size is larger than the cubic matrix. If a fractal dimension exists over a certain size range, then the slope in the log-log plot of the box count vs. box size should be constant, indicating a power law.

The lobar segmentation performed allows for exploration of the distribution of flow rates into the various lobes. By calculating the difference in total volume at full inhalation and exhalation across all 5 lobes, the FVC of the lung can be calculated. By repeating this process for the individual lobes, FVC of the RUL, RML, RLL, LUL, and LLL can also be determined, and by dividing lobar FVC with the overall FVC, lobar ventilation ratios are calculated. These ratios represent the fraction of the total airflow during the breathing cycle that goes to each lobe. Similar to the lobar ventilation ratio, the lobar inflation ratio represents the percentage of an individual lobe's air volume that is inhaled and exhaled during the breathing cycle. It is calculated by dividing the difference in inhalation and exhalation volumes with the inhalation volume. In addition to providing insight as to how air distributes through the lung, these ratios will be necessary for setting appropriate flow boundary conditions in the flow experiments performed.

2.2 Flow experiments

2.2.1 Flow models

From each of the smoking subject groups, one representative subject is selected and used to generate a physical airway model for respiratory flow measurements. For the decliner COPD group, two flow models are generated, both the baseline and 5-year inhalation airway segmentation. For the other groups only the baseline airway inhalation segmentation is used. To design the models, the STL file of the airway volume is first turned into a hollow airway tree with a 2.5 mm thick wall using the software 3-Matics (Materialise, Leuven, Belgium). The distal branches and the trachea are trimmed to allow for outflow and inflow, respectively. Using the software SolidWorks (Mountain View, CA), a plenum is generated to contain the airway tree, and is shaped to fit in the MRI coil used in these experiments. Additionally, this plenum is subdivided into five separate cavities, one for each lobe, each connected to their individual outflow. This is done to control the lobar ventilation when setting flow conditions. The plenum and airway cast are then combined into a single piece. Due to the high geometrical complexity and the material constraint imposed by the MRI technology, the models are 3D printed. In order to accurately print the small distal airways and have hydrodynamically smooth walls, a high-resolution print layer thickness of 100 μm is utilized. Using a material called Watershed XC 11122, the printing is carried out by the W.M. Keck Center (University of Texas El Paso, TX). Figure 4 illustrates the model creation process.

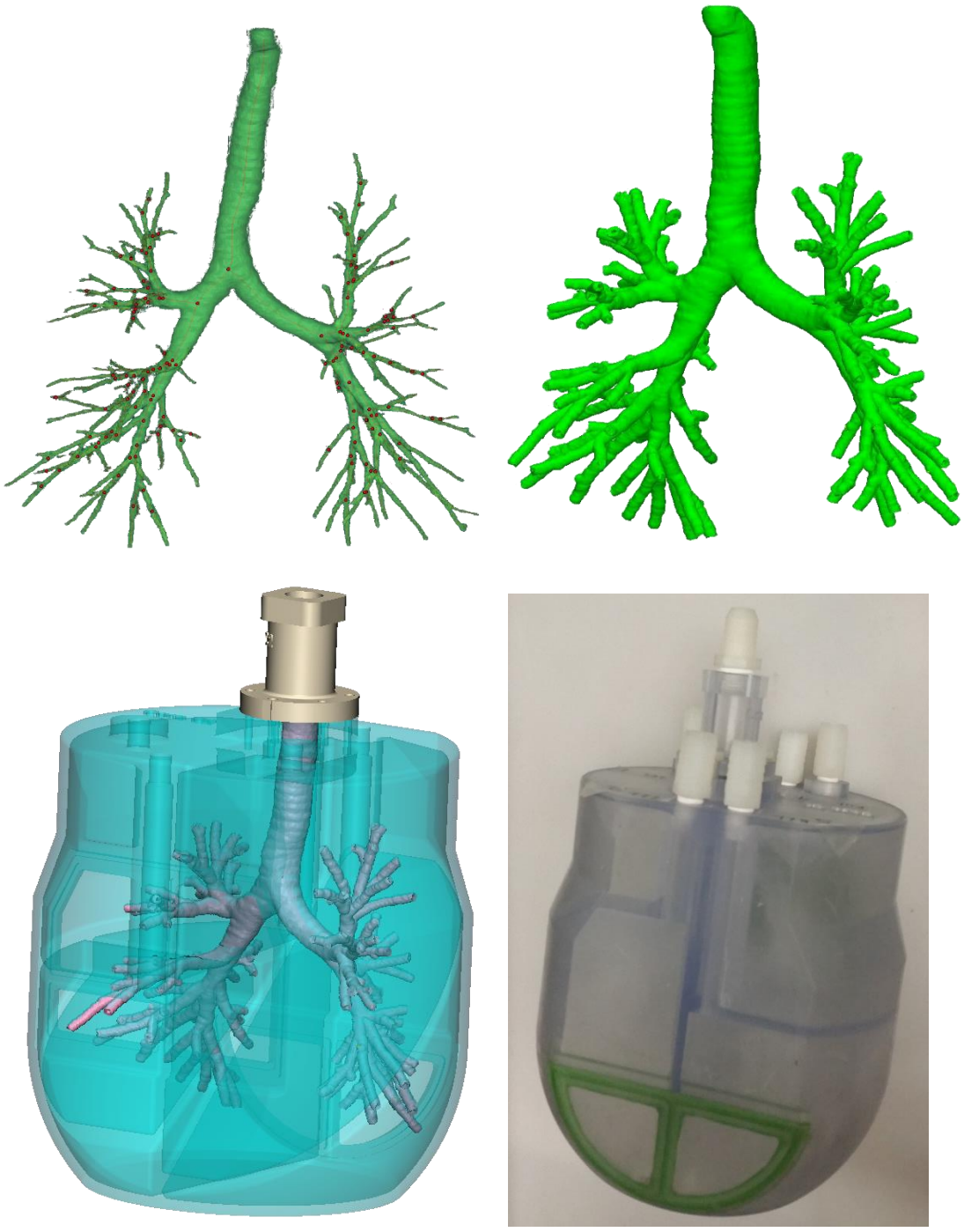

Fig. 4 CAD process of creating the 3D flow models. Upper left: airway tree volume. Upper right: thickened and hollowed airway tree volume. Lower left: CAD generated plenum combined with the hollowed airway volume into one piece. Lower right: 3D printed model with flow loop connectors attached.

2.2.2 Flow experimental setup

The airway flow models are attached to a custom flow loop, illustrated in Figure 5. Using a centrifugal pump (TE-6-MD-SC, Little Giant) and a digital flow regulator (LCR-5PLM-D, Alicat Scientific, Inc), water is pumped from a reservoir through the model inlet and back into the reservoir using plastic tubing of 2.5 cm diameter. The 5 lobar outlets are each connected to 0.9 mm diameter plastic tubing. The relative return flow rates are controlled via 5 needle valves, which are manually set by measuring the individual flow rates of each plenum using a transonic flow meter (Transonic TS410 Tubing Module and Transonic ME-6PXL clamp-on flow probe). These are set to match the lobar flow rates with the calculated lobar ventilation ratios of each subject. All connections and pieces are made of plastic to be MRI compatible.

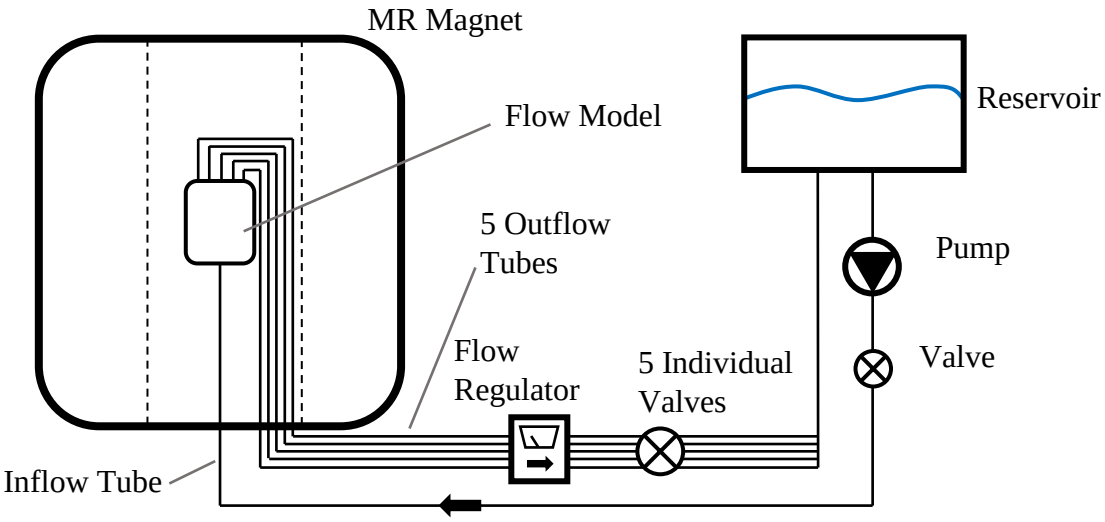

Fig. 5 Diagram of the flow circuit used for MRI velocimetry measurements.

To maximize the MRI signal, a solution of water and copper sulfate (0.06 mol/L) is used as the working fluid. The addition of copper sulfate does not change the fluid properties of water, and significantly increases the MRI signal received, by shortening the water ^{1}H longitudinal relaxation time (T1). Scanning is performed using a 3 Tesla Siemens whole-body scanner at the University of Minnesota Center for Magnetic Resonance Research. The flow model is placed inside a transmit-and-receive radio-

frequency coil typically used for human heads. 3-component 3D velocity fields are acquired using methods described by Elkins et al. (2007), and often referred to as Magnetic Resonance Velocimetry (MRV). The MRI sequence used was the one presented by Markl et al. (2012). To increase accuracy, four consecutive scans are performed and averaged for each model. Scan parameters were set with values as follows in Table 2:

Parameter	**Value**
Repetition time	34.4 ms
Echo time	8.6 ms
Flip angle	35°
Velocity encoding (venc)	0.6 m/s
Resolution	0.6 mm in x, y, and z
Bandwidth	470 Hz/px
Field of view	307 x 230 x 96 mm

Table 2 List of parameters and their values in the MRI sequence used for the flow experiment measurements.

As previously mentioned, deposition of particles occurs mostly during the peak inhalation time of the breathing cycle. To study this, we impose a steady flow rate that matches peak inhalation conditions of normal breathing conditions. Since water is used as the working fluid, we must ensure that dynamic similarity between our experiment and normal breathing of air is ensured. To do this we must match the Reynolds number (Re), which is defined in Equation 1. It is the ratio of inertial forces to viscous forces that a fluid experiences. A larger Re indicates momentum driven flow, while a smaller Re indicates a viscous driven flow. We set the Re of the trachea to ~1800, which is in the

range of peak inhalation for normal breathing. Knowing the viscosity of water and the diameter of our model at the trachea, we impose the flow rate which matches the needed trachea velocity for an Re of 2000. The breathing is also described by the non-dimensional Womersley number (Wo), which relates the oscillating frequency to the viscous forces of a pulsatile flow. However, because we are imposing steady flow, Wo is not relevant to our flow and does not need to be matched for dynamic similarity.

The Reynolds number is defined as:

$$Re = \frac{U_{ax} d}{\nu} \tag{1}$$

where U_{ax} is the mean axial velocity, d is the branch diameter, and ν is the dynamic viscosity of the working fluid.

Chapter 3: Results/Discussion

3.1 Morphological data

3.1.1 Geometrical parameters

Weibel's symmetrical model has a constant h (child to parent diameter ratio) of 2^(-1/3) (≈ 0.79), which theoretically minimizes the resistance and entropy production of the air flow through the airways. As shown in Figure h, the normal smoker and normal non-smoker groups exhibit very stable values of h over all generations and in good agreement with the aforementioned theoretical value. The COPD diseased groups all exhibit values of h lower than the healthy subjects. This translates to the diseased groups having airway shrinkage in comparison to the healthy groups, as visible in Figure 7, where the airway diameter normalized by the trachea diameter is plotted vs. generation in a lin-log plot. Because h is almost constant across all generations, the log of the diameter follows a near linear slope. Interestingly, after 5 years the decliner COPD show a somewhat increased airway diameter, although the differences with respect to the decliner COPD at baseline is only marginally significant.

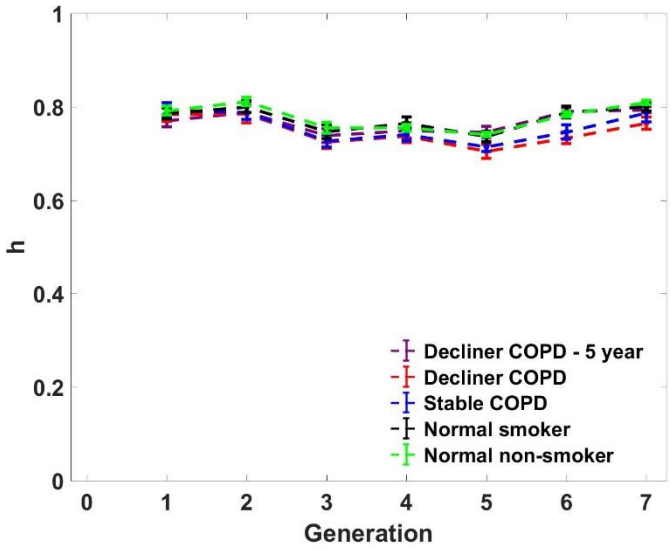

Fig. 6 Homothety parameter, h, vs. generation. Each subject group is averaged over all cases. Error bars reported in standard error.

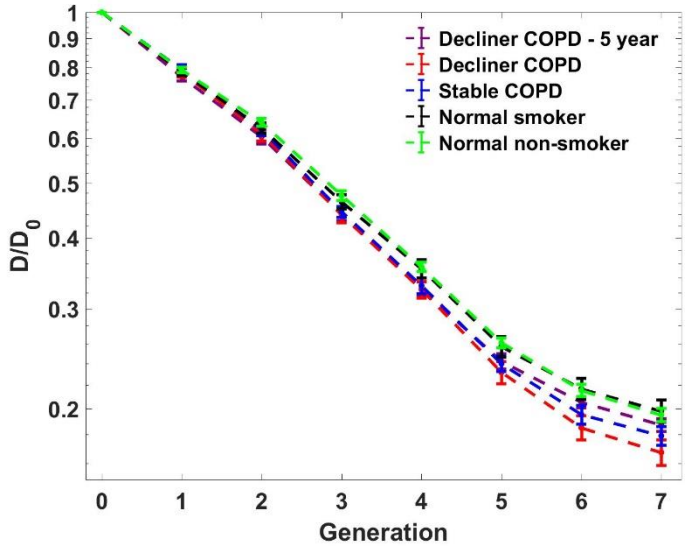

Fig. 7 Lin-log plot of the diameter normalized by trachea diameter vs. generation. Each subject group is averaged over all cases. Error bars reported in standard error.

While Weibel's symmetric model has (by construction) both child airways of equal diameter, this does not hold in actual human anatomy, as reported by Horsfield & Cumming (1968). Figure 8 shows the ratio of diameters of the minor child to major child. With a mean value of 0.85 there is a significant difference in airway size of two sibling branches at each successive generation. Additionally, while the mean value of h over all branches (0.78) matches Weibel's model, when separated into h_{min} and h_{maj}, we find values of 0.71 and 0.85, respectively, shown in Figures 10 and 11. These values are very steady through all generations, indicating that these trends are robust throughout all the airways, and for all groups. Also plotted in Figure 9 is the exponent m described in Table 1, which follows from the assumption that at each branch the flow rate Q is related to the diameter D by the relation $Q = C*D^m$, C being a constant (Murray 1926). The theoretical values for fully developed flows is m = 3 for laminar flow and m = 2.333 for turbulent flows (Uylings 1977). From our morphometric measurements, m remains between these two values for most generations and subject groups, with an average value of 2.4, suggesting that the flow is neither fully laminar nor fully turbulent. Moreover, we shall remind that the theoretical values of the exponent are derived for fully developed flows,

while the present flow is always developing due to the short length-to-diameter ratio of the branched (typically between 1.5 and 5, see below).

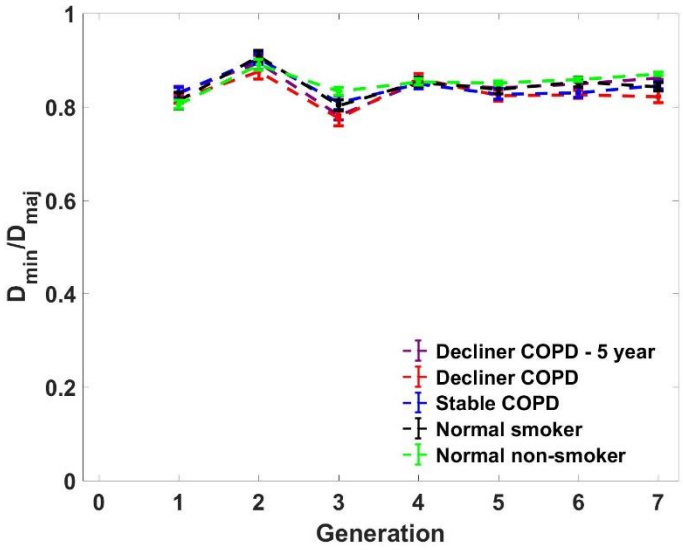

Fig. 8 Ratio of the minor sibling branch diameter to the major sibling branch diameter vs. generation. Each subject group is averaged over all cases. Error bars reported in standard error.

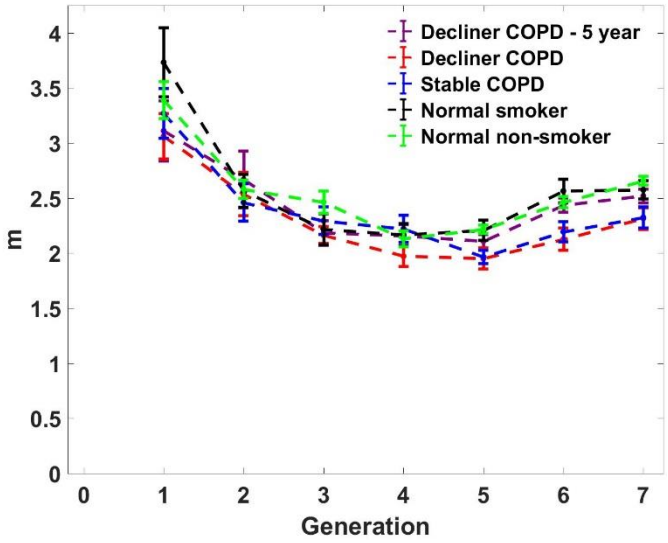

Fig. 9 Exponent m vs. generation. Each subject group is averaged over all cases. Error bars reported in standard error.

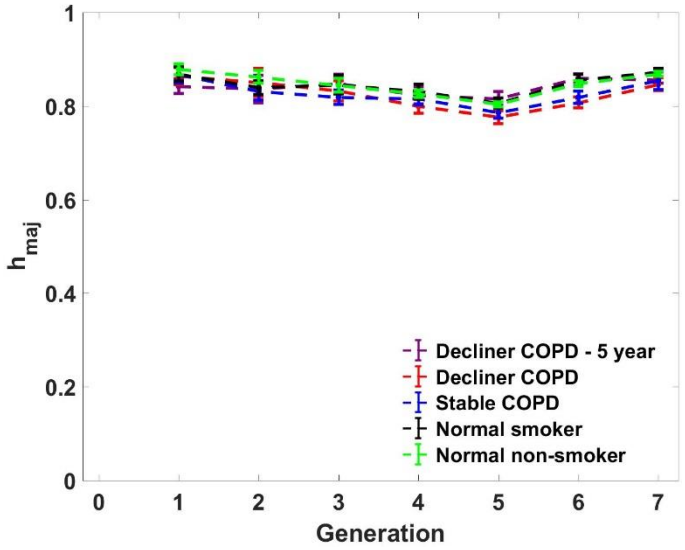

Fig. 10 Major sibling homothety parameter, h_{maj}, vs. generation. Each subject group is averaged over all cases. Error bars reported in standard error.

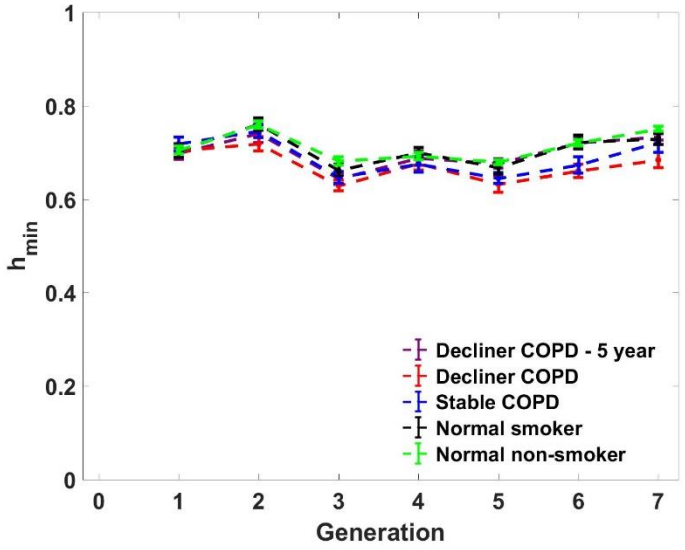

Fig. 11 Minor sibling homothety parameter, h_{min}, vs. generation. Each subject group is averaged over all cases. Error bars reported in standard error.

Figure 12 plots the non-dimensionalized airway length L/D_0 vs. generation number. While showing a decreasing trend from G1 to G4, it stabilizes and remains constant at a value of around 0.75 in the higher generations up to G7. Whether this plateau continues cannot be determined due to the G7 cutoff imposed for resolution

reasons. When combined with the exponential decay of diameter, the trend of L/D does not agree with the classic Weibel model, which postulates a constant value of the L/D ratio. As shown in Figure 13, L/D dips to a low at G2 and G3, but then increases to G7 (due to diameter decreasing while length remains almost constant). This trend is noteworthy because previous studies of tend to report L/D as a single value averaged over all branches at ~3 (Sapoval et al. 2002, Tawhai et al. 2004). Therefore it may be more meaningful to report findings and trends of L/D vs. generations rather than as a single value. When comparing the 5 subject groups, we find that the stable COPD and decliner COPD show significantly higher values of L/D, especially in G4 and deeper. Similar to the D/D_0 findings, the decliner COPD – 5 year group tends to behave more like the healthy control groups than its COPD counterparts. L/D appears to be a potential bio-marker for assessing disease susceptibility, but may not be well suited for late-stage COPD diagnosis.

While the ratio of sibling diameters is found to be in the range of previously found values, the behavior of the ratio of sibling length is surprising. L_{min}/L_{maj} is plotted in Figure 14, and shows that the minor sibling consistently is more than twice as long as the major sibling for all cases. This is further shown by Figure 15, in which a negative correlation between D_{min}/D_{maj} and L_{min}/L_{maj} is evident. This indicates that, in general, the bifurcations include a thicker and shorter airway and a thinner but longer one.

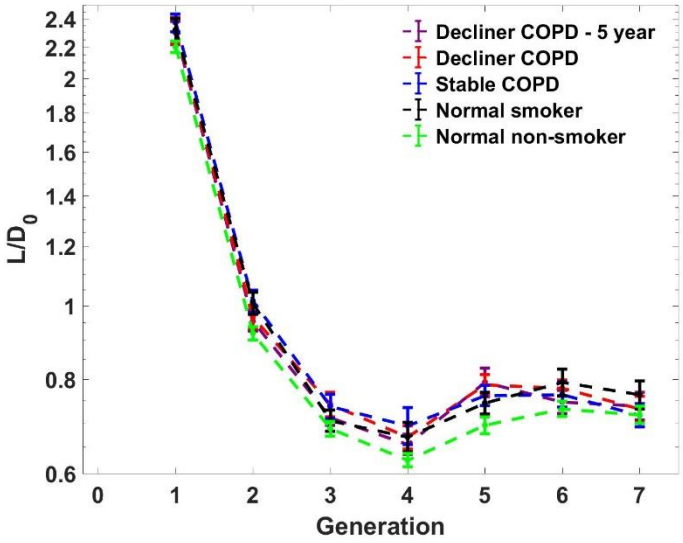

Fig. 12 Lin-log plot of the branch length normalized by trachea diameter vs. generation. Each subject group is averaged over all cases. Error bars reported in standard error.

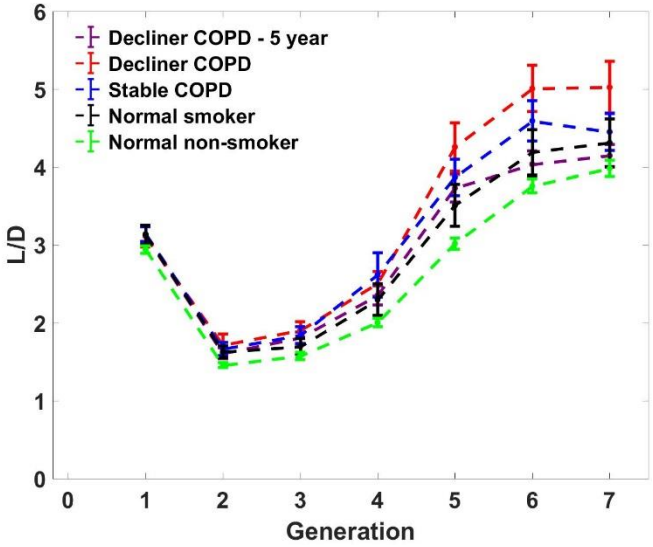

Fig. 13 Branch length over diameter ratio vs. generation. Each subject group is averaged over all cases. Error bars reported in standard error.

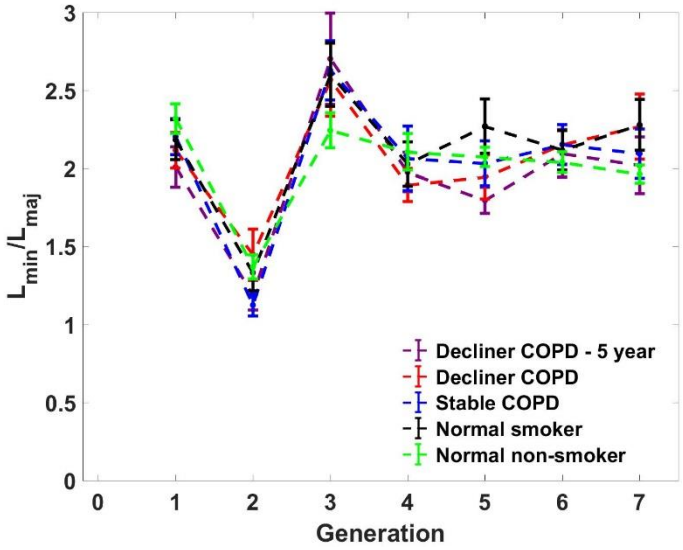

Fig. 14 Ratio of the minor sibling branch length to the major sibling branch length vs. generation. Each subject group is averaged over all cases. Error bars reported in standard error.

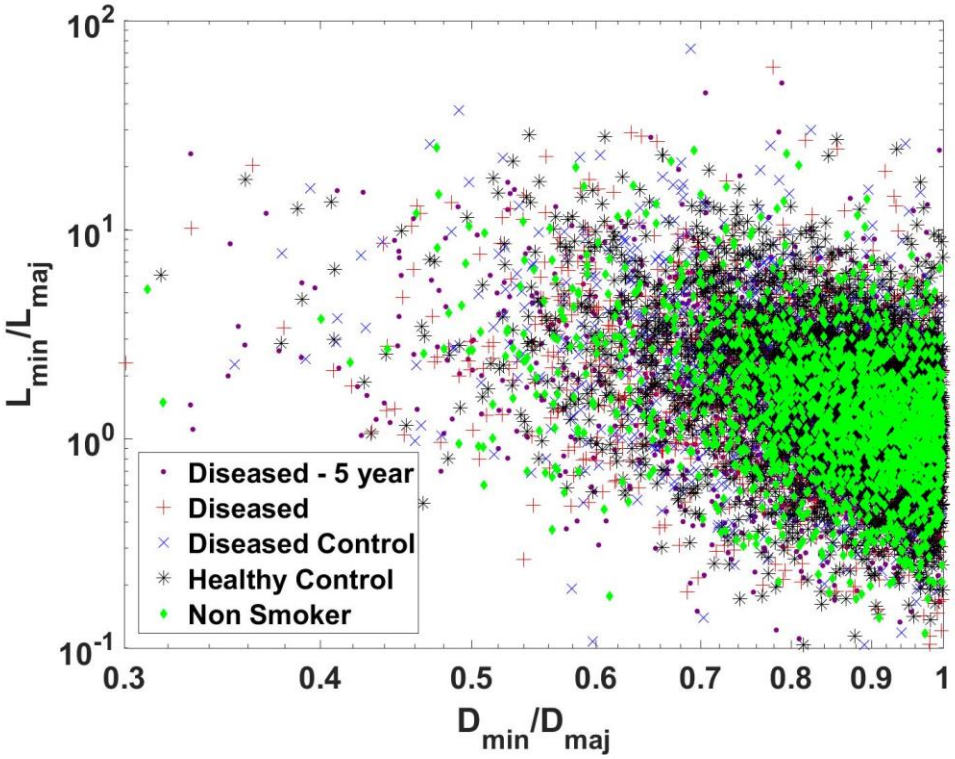

Fig. 15 Log-log scatter of the ratio of the minor sibling branch diameter to the major sibling branch diameter vs. the ratio of the minor sibling branch diameter to the major sibling branch diameter.

The direction of a branch relative to its parent and parent's sibling can be described with 3 angles: the branching angle θ, the rotation angle ϕ, and the inclination angle δ. These are described in detail in Table 1 and Figure 3. The total branching angle θ is very consistent across all subject groups, with a mean value of 66°, which matches the previous findings of Weibel (1963). The results show a decreasing trend in the deeper generations but appears to start plateauing in G5-G7, as shown in Figure 16. The individual branching angles, θ_{min} and θ_{maj} are shown in Figures 17 and 18, respectively. θ_{min}, associated with the sibling of smaller diameter, is consistently larger than θ_{maj} across all subject groups, by an average of approximately 6°. It is also found that between 60% and 62% of all pairs of siblings have a larger θ_{min} than θ_{maj}. This relationship is further explored by examining the ratio of $|\theta_{min} - \theta_{maj}|/\theta$, which describes the relative difference in sibling branching angle while accounting for the total branching angle. As shown in Figure 19, this ratio peaks at G2 with a value of approximately 0.65, then plateaus at further generations at a value of approximately 0.4. The asymmetry of the branching angles makes sense from a fluid mechanics point of view. Because the larger diameter branch will contain a larger percentage of the incoming flow, a sharper turn would create more air resistance than it would in the smaller sibling.

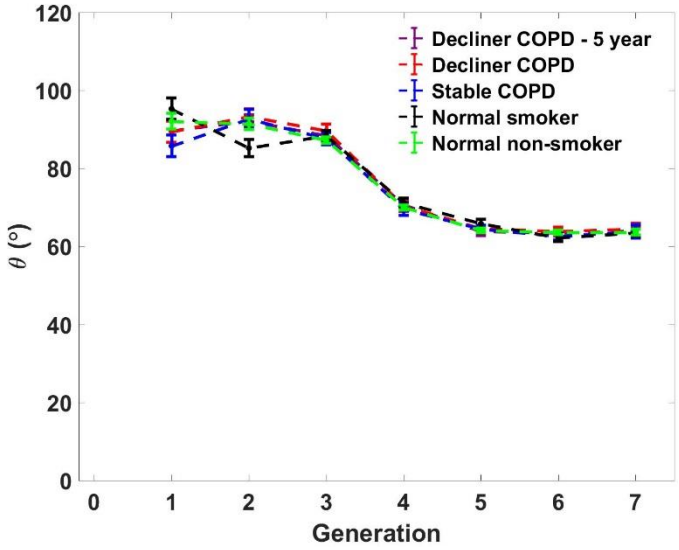

Fig. 16 Branching angle vs. generation. Each subject group is averaged over all cases. Error bars reported in standard error.

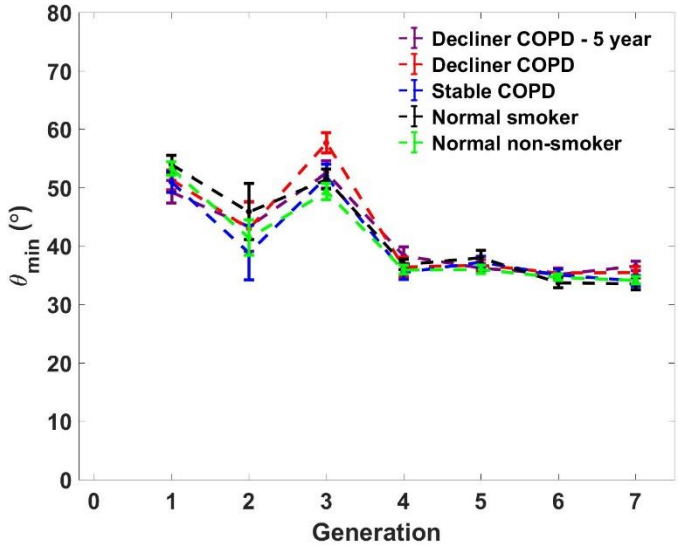

Fig. 17 Minor branching angle vs. generation. Each subject group is averaged over all cases. Error bars reported in standard error.

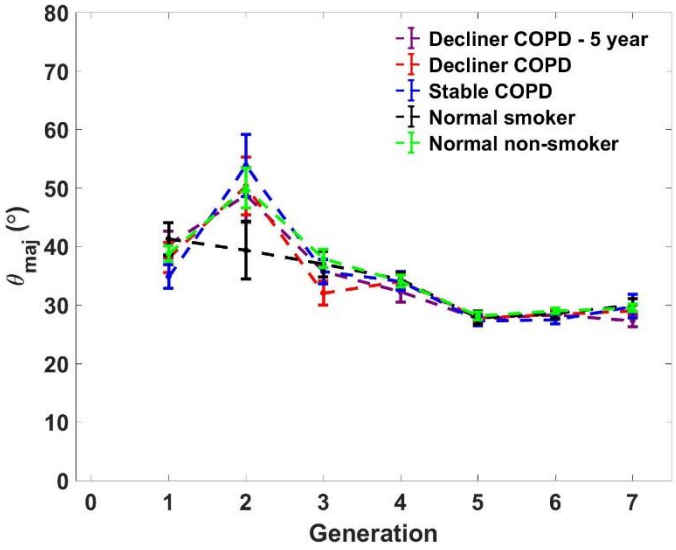

Fig. 18 Major branching angle vs. generation. Each subject group is averaged over all cases. Error bars reported in standard error.

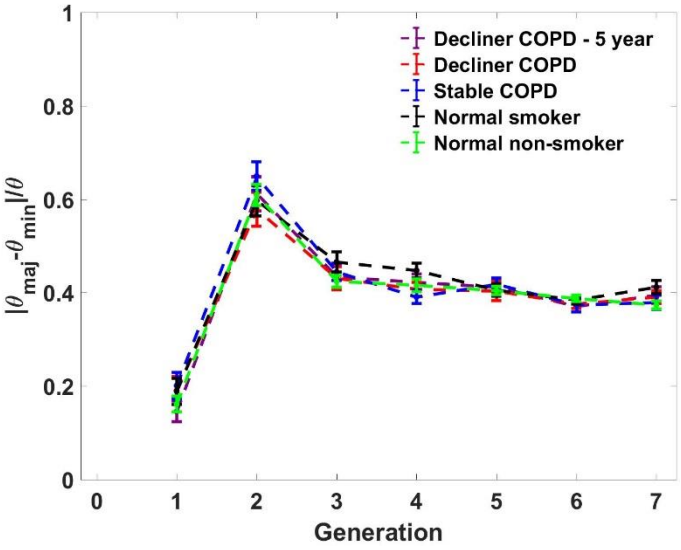

Fig. 19 Ratio of the difference in major and minor branching angles divided by the total branching angle vs. generation. Each subject group is averaged over all cases. Error bars reported in standard error.

The rotation angle ϕ and inclination angle δ are plotted vs. generation in Figure 20. ϕ is found to be consistent across all subject groups with a mean value of 54°. This is significantly smaller than reported findings by Tawhai et al. 2004 and Sauret et al. 2002,

who report values of 76° and 79°, respectively, but only examining one subject each. δ is found to be quite small and consistent across all generations and subject groups. Most studies and theoretical models assume this angle to be 0°, this study confirms that it takes on very small angles with a mean of less than 8°.

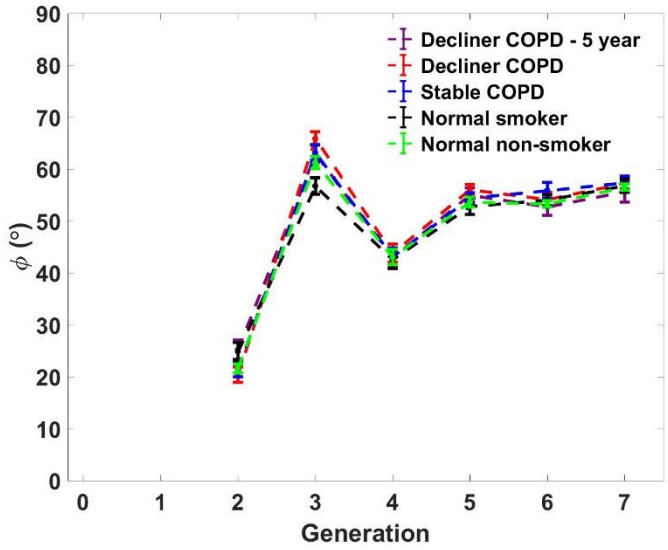

Fig. 20 Branch rotation angle vs. generation. Each subject group is averaged over all cases. Error bars reported in standard error.

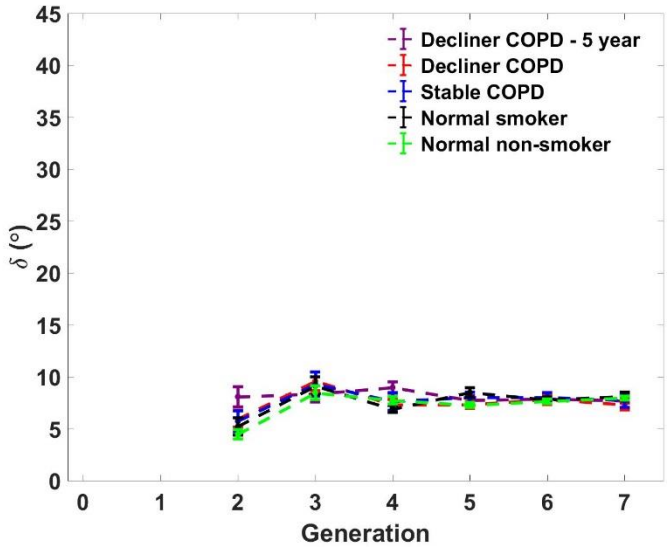

Fig. 21 Branch inclination angle vs. generation. Each subject group is averaged over all cases. Error bars reported in standard error.

Parameter Mean ± SD	**Overall**	**COPD Decliner 5 yr**	**COPD Decliner baseline**	**Stable COPD**	**Normal Smoker**	**Normal Non-Smoker**
# branches	176 ± 33	167 ± 31	172 ± 32	165 ± 38	173 ± 27	192 ± 31
D (mm)	4.80 ± 2.74	4.87 ± 2.67	4.68 ± 3.00	4.73 ± 2.89	5.02 ± 2.72	4.75 ± 2.58
D/D_0	0.25 ± 0.14	0.25 ± 0.14	0.24 ± 0.15	0.25 ± 0.15	0.27 ± 0.14	0.26 ± 0.14
L (mm)	15 ± 12	15 ± 12	16 ± 12	15 ± 12	15 ± 12	14 ± 11
L/D_0	0.78 ± 0.62	0.80 ± 0.61	0.81 ± 0.63	0.80 ± 0.64	081 ± 0.66	0.75 ± 0.59
L/D	3.7 ± 3.0	3.6 ± 2.7	4.3 ± 3.7	3.9 ± 3.2	3.7 ± 3.2	3.4 ± 2.6
$(L/D)_{min}$	4.6 ± 3.3	4.4 ± 2.8	5.3 ± 4.0	4.9 ± 3.5	4.7 ± 3.5	4.3 ± 2.8
$(L/D)_{maj}$	3.0 ± 2.6	3.0 ± 2.5	3.4 ± 3.1	3.2 ± 2.6	2.8 ± 2.6	2.8 ± 2.3
L_{min}/L_{maj}	2.1 ± 2.5	1.9 ± 2.2	2.1 ± 2.8	2.1 ± 2.8	2.2 ± 3.1	2.0 ± 2.1
h	0.78 ± 0.16	0.78 ± 0.16	0.75 ± 0.18	0.75 ± 0.17	0.79 ± 0.16	0.79 ± 0.15
h_{min}	0.71 ± 0.14	0.72 ± 0.13	0.68 ± 0.15	0.69 ± 0.14	0.72 ± 0.14	0.73 ± 0.13
h_{maj}	0.85 ± 0.16	0.85 ± 0.16	0.83 ± 0.17	0.85 ± 0.17	0.86 ± 0.16	0.86 ± 0.15
m	2.4 ± 1.1	2.4 ± 1.0	2.2 ± 1.1	2.3 ± 1.1	2.5 ± 1.1	2.5 ± 1.1
D_{min}/D_{maj}	0.85 ± 0.12	0.85 ± 0.12	0.83 ± 0.13	0.84 ± 0.13	0.5 ± 0.12	0.86 ± 0.11
θ [°]	66 ± 20	66 ± 19	66 ± 20	65 ± 20	66 ± 19	66 ± 20
θ_{min} [°]	36 ± 18	37 ± 18	37 ± 18	36 ± 18	35 ± 18	36 ± 18
θ_{maj} [°]	30 ± 20	30 ± 19	29 ± 19	29 ± 19	31 ± 20	31 ± 20
$\lvert\theta_{min} - \theta_{maj}\rvert/\theta$	0.40 ± 0.25	0.40 ± 0.24	0.40 ± 0.25	0.39 ± 0.25	0.41 ±0.25	0.39 ± 0.25
$\theta_{min} > \theta_{maj}$	61%	62%	62%	62%	60%	60%
ϕ [°]	54 ± 26	53 ± 26	54 ± 26	54 ± 27	53 ± 26	54 ± 26
δ [°]	7.8 ± 6.8	7.8 ± 6.6	7.5 ± 7.0	7.7 ± 6.9	8.1 ± 7.0	7.8 ± 6.8

Table 3 List of the values of the various geometrical parameters over all generations analyzed (G0-G7) for each subject group and all groups combined. Error reported in standard deviation.

3.1.2 Fractal Analysis

Using the box counting method described in section 2.1.3, the fractal dimension of the 3D airway volume was explored. Figure 20 plot the box size r vs. box count n for each subject group. All cases exhibit a very linear relationship in the log-log plot for over a decade in box sizes, indicating that they all have a regular and constant fractal dimension over the scales analyzed. The slope of these log-log lines is the fractal dimension, which is shown for each case in Figure 23. The normal non-smoker subjects have the highest fractal dimensions, with a value of 1.89. The normal non-smoker, stable COPD, and decliner COPD (baseline), steadily decrease in fractal dimension, with the decliner COPD having a fractal dimension of 1.83. The decliner COPD at 5 years appears to return to normal smoking levels with a fractal dimension of 1.86, suggesting that the onset of COPD may result in changes in the airways. These changes are likely due in large part to the decreasing D and increasing L/D values we observe in diseased cases. However, other geometrical factors that may not have been captured by our centerline analysis may also play an important role in the changing fractal dimension. Interestingly, the fractal dimension trend also suggests that structural changes in the airway tree correlate better with future progression than with the present status of the disease. This lends credibility to the assumption that airway anatomy and consequent flow features are among the causes of the disease inception and progression.

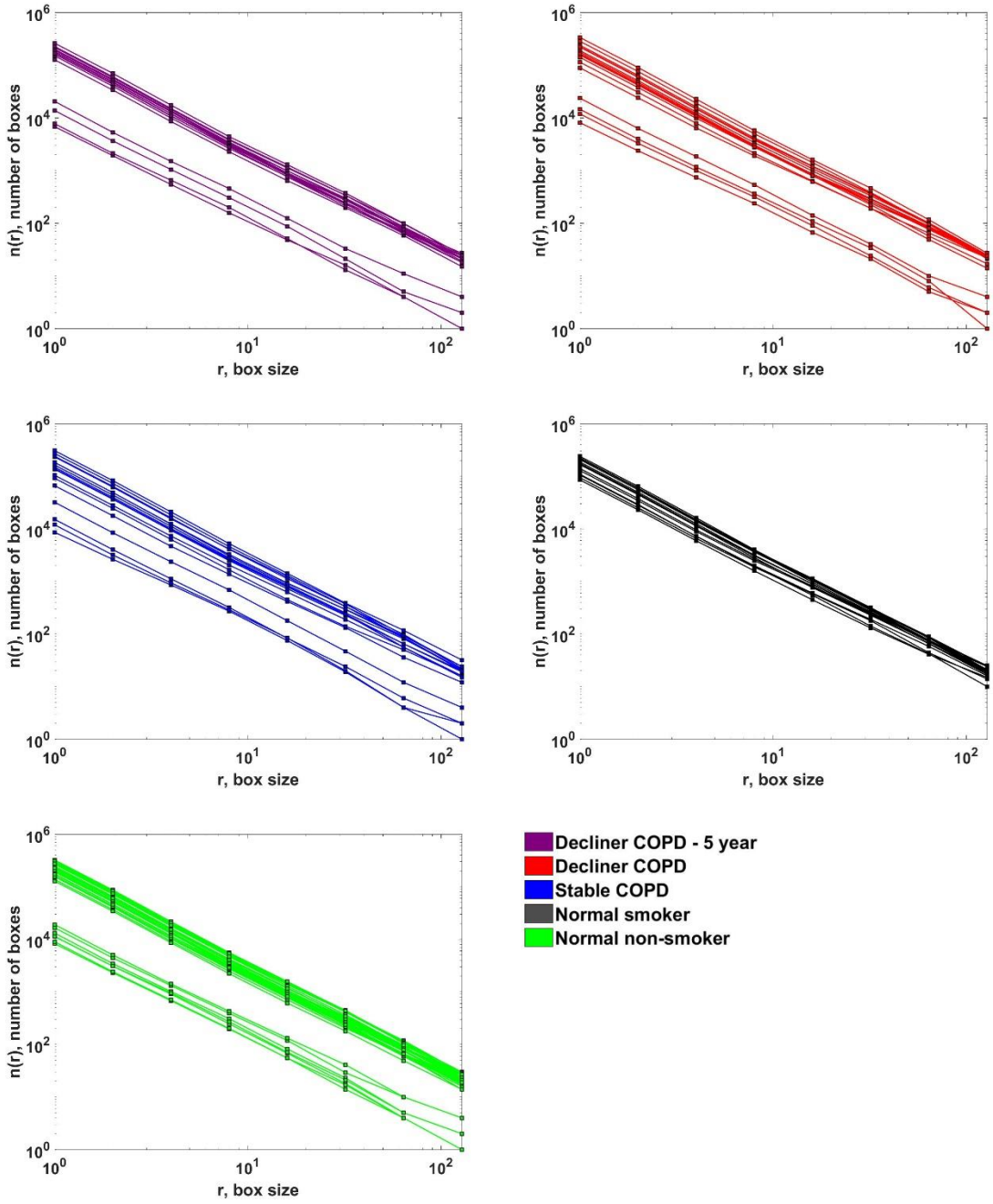

Fig. 22 Log-log box counting plots of n vs. r for each subject group, each line is a specific subject airway volume. Top left: decliner COPD – 5-year. Top right: decliner COPD. Middle left: stable COPD. Middle right: normal smoker. Bottom: normal non-smoker.

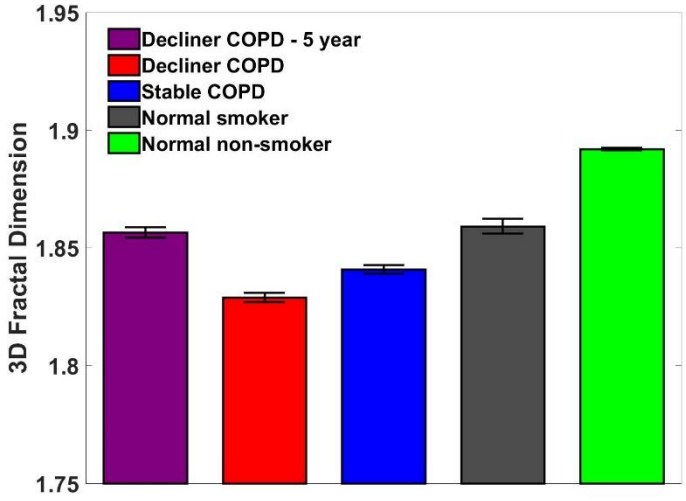

Fig. 23 Fractal dimension calculated from the slope of the box counting method. Error bars reported in standard error.

3.2 Inhalation flow data

3.2.1 Lobar ventilation

CT scan segmentation allowed for reconstruction of lobar volumes at both inhalation and exhalation. Due to typically lower scan quality for exhalation than inhalation, not all exhalation volumes were successfully segmented, leading to less usable subjects in each group. The decliner COPD – 5 year, decliner COPD, stable COPD, normal smoker, and normal non-smoker have 9, 15, 16, 15, and 12 subjects with successful lobar volume segmentation, respectively. From these volumes, the lobar ventilation ratios were calculated and are reported in Figure 24, as averages over each group of subjects. All groups report very consistent values for each of the five lobes. Notably, the Right Lower Lobe is typically the most ventilated lobe, followed by the Left Lower Lobe, Left Upper Lobe, and the Right Upper Lobe in that order. The Right Middle Lobe is the least ventilated one (being also by far the smallest in size), with ventilation approximately 5-6 times smaller than the Left Upper Lobe. Figure 25 displays the lobar inflation ratios, i.e. the difference in peak inhalation volume to exhalation volume

normalized by the peak inhalation volume. Typically, lobes do not deflate past 55% of peak volume, with the Right Lower Lobe and Left Lower Lobe having the highest inflation ratio values between 0.45 and 0.55. The Right Middle Lobe has the smallest inflation ratio value between 0.3 and 0.35 between the various groups. While the decliner COPD baseline group may have higher inflation ratios for the Right Lower Lobe than the other groups, no stark differences in ventilation or inflation ratios appear across all groups.

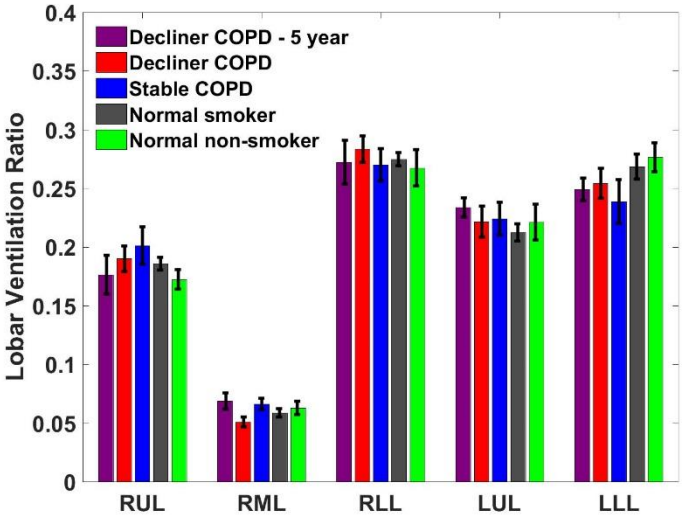

Fig. 24 Lobar ventilation ratios. Error bars reported in standard error.

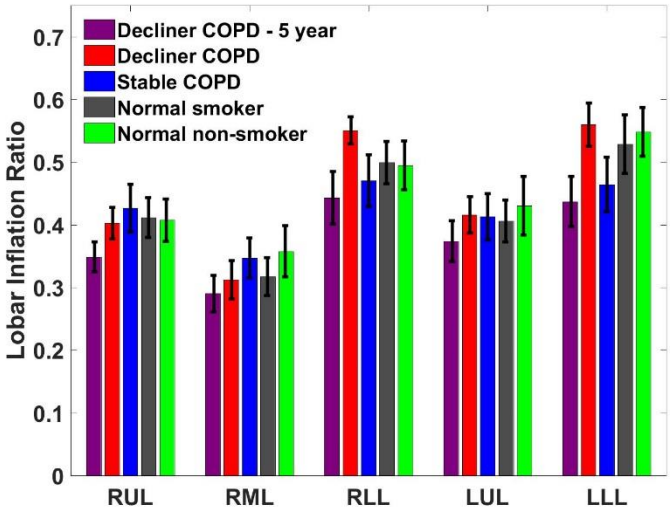

Fig. 25 Lobar inflation ratios. Error bars reported in standard error.

3.2.2 Inhalation flow experiments

Using MRI, the 3D 3-component velocity fields of the airways of each model were acquired for steady inhalation. An inlet condition was imposed by setting the tracheal Reynolds number Re ~ 1800 in each case to match peak inhalation of normal breathing patterns. The subject specific lobar ventilation imposed at the outlets for each model is shown in Figure 26. Once the data is acquired, a mask is imposed on the data to capture the flow exclusively in the airways since the flow in the plena is of no interest to this study. Figure 27 shows various slices of the flow field acquired for one of the subjects, illustrating the 3D capabilities and resolution of the Magnetic Resonance Velocimetry (MRV) results.

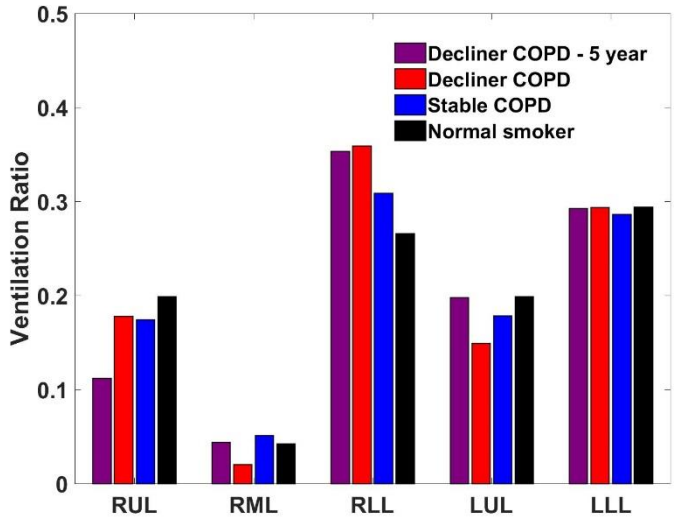

Fig. 26 Lobar ventilation ratios imposed for each flow model, calculated from the segmented lobar volumes.

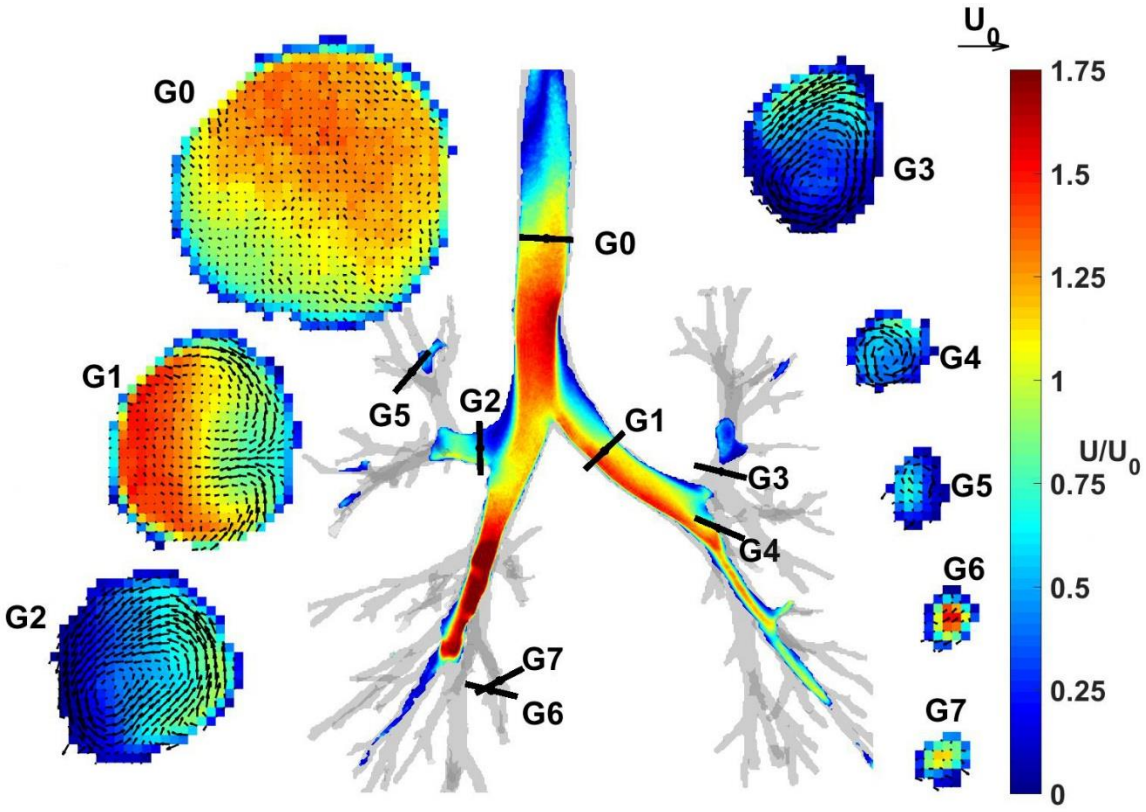

Fig. 27 Stream-wise and secondary velocity contours at various generations throughout the airway tree of the normal smoker subject flow model. All velocities normalized by the bulk trachea velocity.

To analyze the stream-wise and secondary flows, the centerline of the mask is computed using Mimics. From this, various flow parameters can be computed at any point along the centerline. The centerline information includes the tangent vector to the path at every point, that can be used to create slices that capture secondary flows (U_{sec} in Figure 28). The geometrical tangent, however, is not necessarily the same as the stream-wise flow direction. For a direction to be truly stream-wise, the in-plane mass flux of a cross-section must be zero. Therefore, first the relative in-plane mass flux (normalized by the stream-wise mass flux, C parameter in Eq. X below) is calculated along the cross-section normal to the geometric centerline tangent.

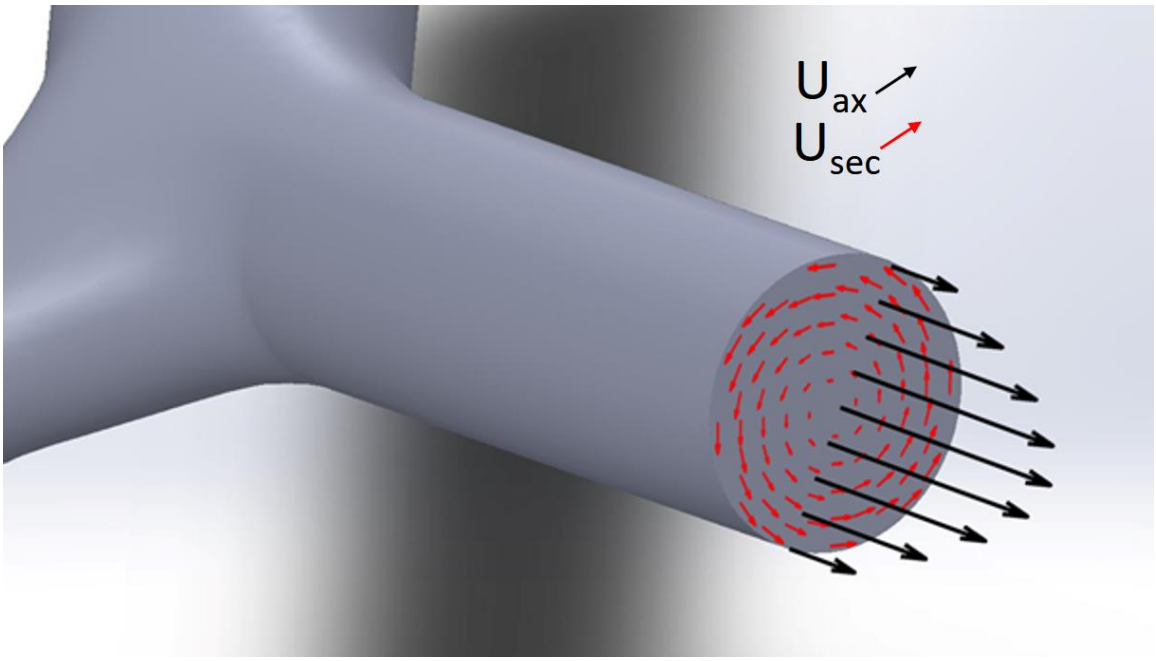

Fig. 28 Illustration of stream-wise velocity U_{ax} and secondary velocity U_{sec} in a branch.

$$C = \frac{|\sum v| + |\sum w|}{|\sum u|} \tag{2}$$

In Eq. 1, u is the out-of-plane (stream-wise, or axial) velocity, and v and w are the in-plane (secondary) components. If C exceeds a small threshold, a simple minimization routine is utilized to find an alternative direction that satisfies such threshold. Here we use a threshold of 0.03, and search within a solid angle of 30° from the geometric centerline, with steps of 0.5°. In-plane (U_{sec}) and out-of-plane (U_{ax}) flow is illustrated in Figure 28. Small variations in the threshold (e.g., 0.01 instead of 0.03) and the angle search parameters return qualitatively and quantitatively similar results. Resulting values of the continuity parameter are plotted vs. generation in Figure 29. Continuity is typically very well conserved in all selected branches, with a mean C parameter value of ~0.005.

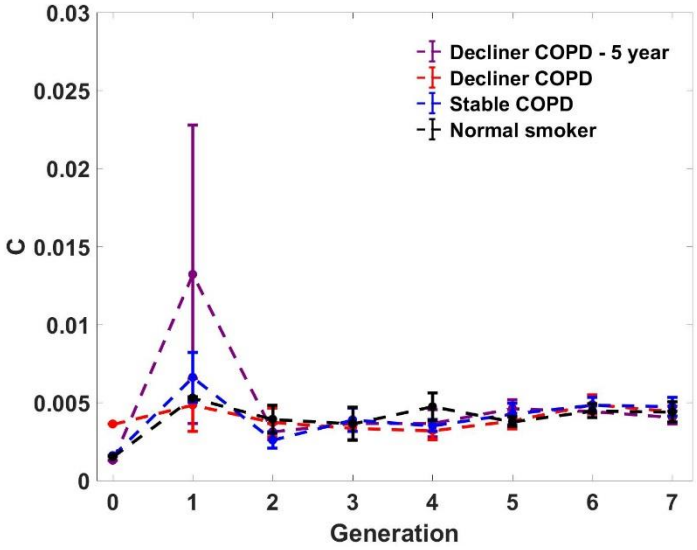

Fig. 29 Continuity flow parameter vs. generations. Averages over each generation calculated for each subject. Error bars reported in standard error.

With the stream-wise direction determined, a series of flow parameters can be defined and calculated in a local frame of reference along the centerline. These are listed and explained in Table 4. For each branch, parameter values are calculated by averaging the middle 50% of the branch length (defined by connecting successive bifurcation points). This is done to avoid points in the bifurcation regions (where the stream-wise direction is not trivial to define univocally).

Parameter	Description
U_{ax} (m/s)	Mean stream wise velocity
U_{sec} (m/s)	Mean in-plane velocity magnitude
U_{ax}/U_{sec}	Ratio of the out-of-plane to stream wise velocity
Q	Flow rate
Re	Reynolds number (see Equation 1)
D parameter	Momentum distortion parameter (see Equation 3)
E parameter	Secondary flow parameter (see Equation 4)
C	Continuity flow parameter (see Equation 2)

Table 4 List of the values of the various flow parameters analyzed for each subject using the MRI flow data and the extracted centerline of the MRI data mask.

The D and E parameters are defined as (Banko et al. 2015)

$$D = \frac{\int_A (\vec{u}\cdot\hat{n})^2 dA}{Q^2/A} - 1 \tag{3}$$

$$E = \left\{ \frac{\int_A [\vec{u} - (\vec{u}\cdot\hat{n})\hat{n}]^2 dA}{\int_A (\vec{u}\cdot\hat{n})^2 dA} \right\}^{\frac{1}{2}} \tag{4}$$

where A is the cross-sectional area, $\vec{u}$ is the velocity vector, $\hat{n}$ is the unit vector normal to the branch cross-section. The D parameter represents the relative difference between the stream-wise momentum flux of the actual flow and that of a plug flow carrying the same mass flow rate. The E parameter represents the relative strength of secondary velocity components to the stream-wise velocity components over each cross-section.

The imposed inlet Reynolds number at the trachea (as prescribed by the Alicat flow regulator) is generally well recovered by the MRV measurements as shown in Figure 30. Additionally, continuity dictates that, if the proportions of the symmetric model of Weibel are respected, Re for the child branches will be 2h times smaller than the parent's Re. Figure 30 plots the log of Re superimposed with this ideal curve (a

straight line in a lin-log plot), using a value of h = 0.78. The data is in very good agreement with this relationship for all cases.

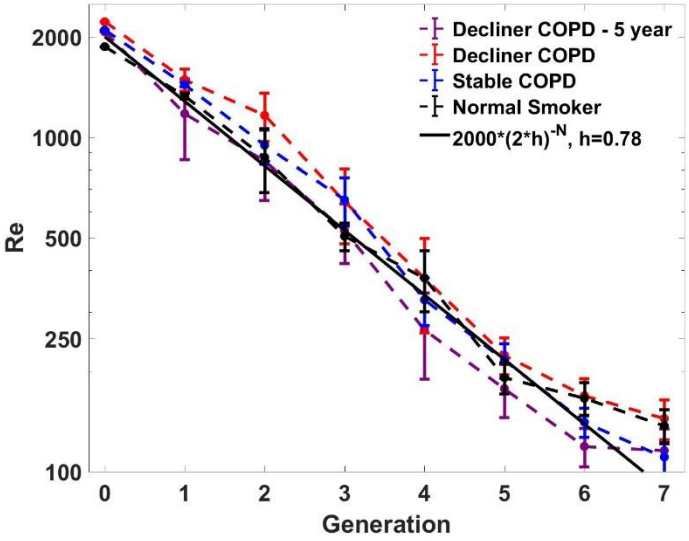

Fig. 30 Lin-log plot of Reynolds number vs. generations. Averages over each generation calculated for each subject. Also plotted is the theoretical Reynolds number behavior in a symmetric dichotomous model with child-to-parent diameter ratio of 0.78, the average value found in this work. Error bars reported in standard error.

Figure 31 shows the secondary flow magnitude normalized by the stream-wise velocity at the trachea (U_0). We can consider this quantity an "absolute" intensity of the secondary flows. This in general grows up to about $0.15U_0$ at between G2 and G3, and then progressively dissipates through the deeper generations. On the other hand, the secondary flow magnitude normalized by the local axial velocity (which can be thought of as a "relative" secondary flow intensity) grows up to about $0.25U_{ax}$ around G3 where it reaches a plateau. This is shown in Figure 32. Studies using idealized models such as Horsfield (1971) and Weibel (1963) found secondary flows typically not exceeding 0.16 (Isabey & Chang 1982) and 0.1-0.2 (Fresconi & Prasad 2007), respectively.

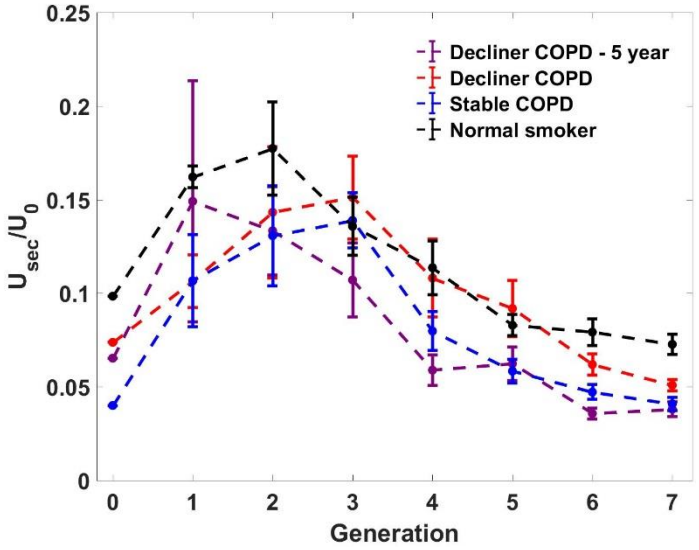

Fig. 31 Secondary flow magnitude normalized by bulk trachea velocity vs. generations. Averages over each generation calculated for each subject. Error bars reported in standard error.

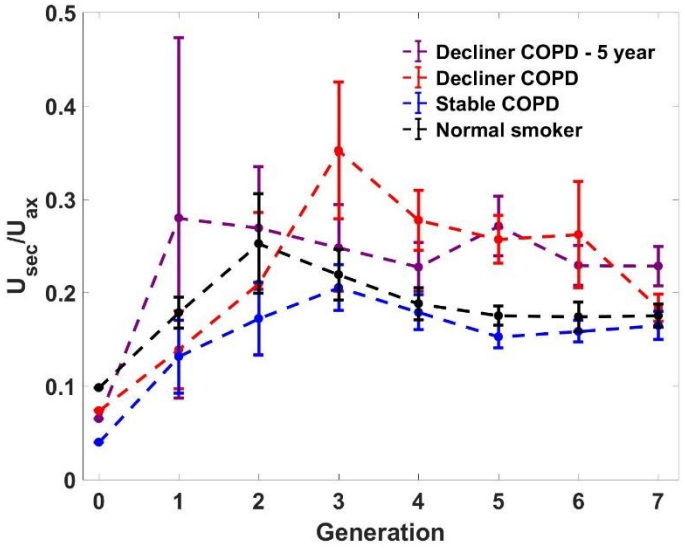

Fig. 32 Secondary flow magnitude normalized by local axial velocity vs. generations. Averages over each generation calculated for each subject. Error bars reported in standard error.

Padilla (2012) introduced the distortion parameter D, calculated using Equation 3. This value is useful in quantifying the stream-wise velocity variation along a cross-section normal to the stream wise direction of the flow. This parameter relates to the

longitudinal dispersion (Fresconi and Prasad 2007), i.e. the ability of the flow to induce diffusion of an inhaled bolus by stretching it along the direction of the flow. In a round pipe, plug flow has a D parameter value of 0, while a fully developed laminar flow has a D parameter value of 1/3 and a fully developed turbulent flow has a D parameter value of 0.02. As shown in Figure 33, we find that the D parameter typically increases over the first few generations. This trend is consistent with the flow becoming more laminar in deeper generations, as per the decreasing Re trend. The decliner COPD – both at baseline and after 5 years – have greater values than the controls up to G4, but the large error bars indicate strong variation between branches in the same generation, and therefore limit somewhat the conclusiveness of this trend. The values found are in the range of those found in Jalal et al. (2016), which studied the idealized Weibel model exploring G0-G2 with 3D MRI velocimetry: for an inlet Re of 2000, they found values of D ranging from 0.2 to 0.6 in G0-G2.

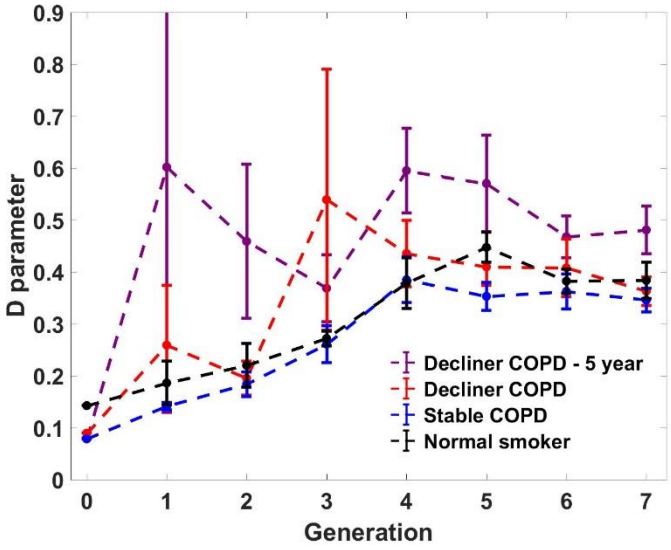

Fig. 33 Distortion parameter D vs. generation. Averages over each generation calculated for each subject. Error bars reported in standard error.

Banko et al. (2015) introduced a secondary flow strength parameter E, defined in Equation 4. This parameter relates to the lateral dispersion (Fresconi & Prasad 2007), i.e., the ability of the flow to induce diffusion of an inhaled bolus by stirring it along planes perpendicular to the main flow direction. The study reported values of E between 0.05

(G0) and 0.51 (G2) in a 3D subject specific model of airways analyzed using MRI velocimetry. Jalal et al. (2016) report values with a maximum of 0.07 in their Weibel model study. The values are plotted in Figure 34, and closely agree with Banko's findings on a healthy subject. We report low values between 0.03 and 0.1 at G0 and values varying around 0.25 in the deeper airways (G2-G7). E peaks at G2 and G3 before slowly but steadily decreases up to G7 for all subject groups. The decliner COPD group (5 year and baseline) have values of E significantly greater than the control groups, which suggests that COPD airways induce more secondary flows than healthy lungs. These findings indicate that higher intensity secondary flows may be a biomarker or predictor of COPD. Both D and E parameters are strongly related to how particles progress and deposit throughout the airways for they quantify the distortion magnitude of flow both in the streetwise and in-plane directions. Changes found in these parameters between heathy and diseased airways show that particles will deposit in the airways differently, and deeper generation particle deposition (from smoking, pollution, etc.) is the biggest risk factor associated with COPD.

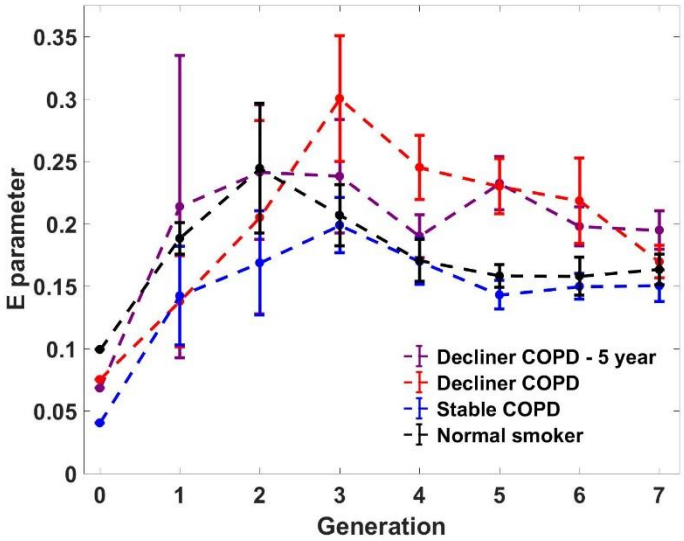

Fig. 34 Secondary flow energy parameter E vs. generation. Averages over each generation calculated for each subject. Error bars reported in standard error.

Figures 35 and 36 plot the evolution of parameters D and E from the trachea to selected paths in the LUL and LLL. Both E and D remain constant in the trachea, before

spiking up when approaching the G0 carina. While D retains its G0 value in G1, E significantly increases. Past G1, D tends to steadily increase, suggesting that the flow behaves in a more laminar-like way in the deeper airways, at least in terms of stream-wise velocity profile. E becomes relatively strong in G1-G5, but decreases to near trachea levels in G6 and G7. Jalal et al. (2016) similarly tracked values of D and E in G0-G2 of the Weibel model. They found similar values of D in G0, although report values as high as 0.58 in G1, compared to 0.4 here. They also find a similar trend of decreasing D from the beginning to end of the G1 branch. Here we find similar trends of E parameter as in Jalal et al., peaking at the beginning of a branch (just after the carina region) and steadily decreasing until the next carina. However, they report much lower values of E, with maximums of 0.07 and 0.06 in G1 and G2, respectively, compared to near 0.4 here.

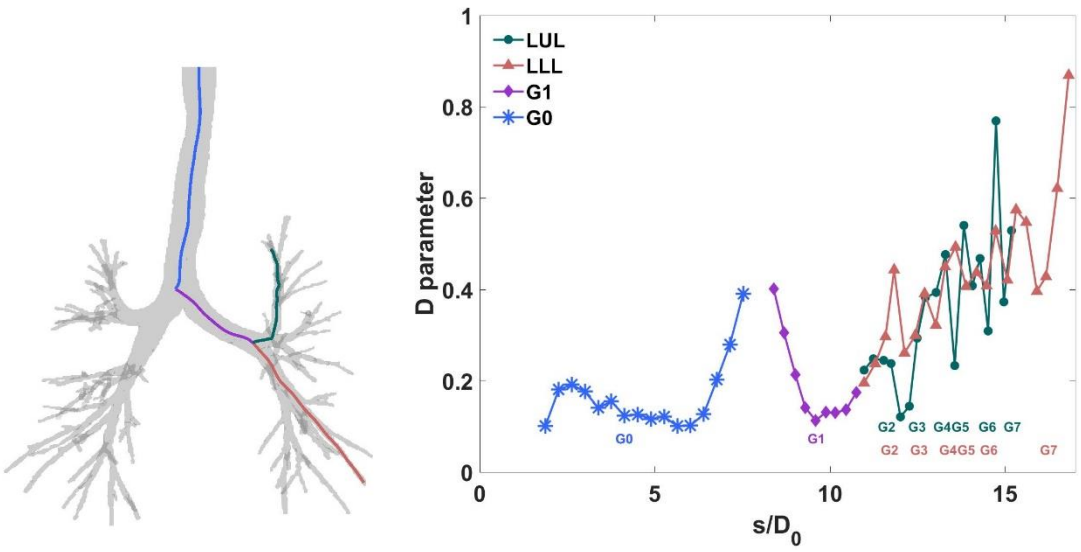

Fig. 35 Distortion parameter D vs. path length normalized by trachea diameter for the normal smoker subject. Path shown on left.

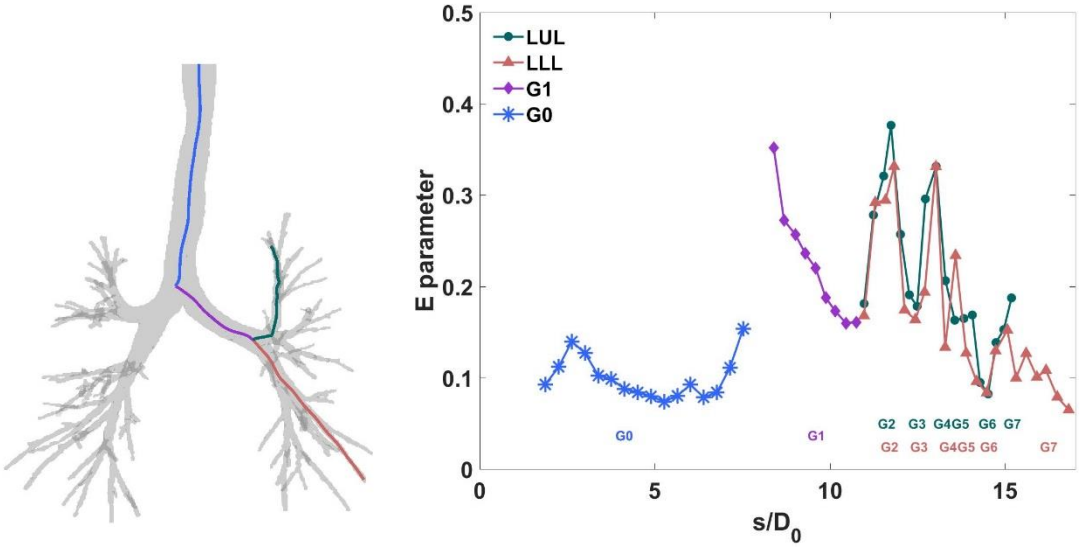

Fig. 36 Secondary flow energy parameter E vs. path length normalized by trachea diameter for the normal smoker subject. Path shown on left.

Figure 37 shows the average branch stream-wise flow rate per generation. All subject groups follow the expected trend of exponential decay with branching generation due to the dichotomous nature of the airways. This is further confirmed in Figure 38, which plots branch flow rate vs. branch diameter. The power law of $Q = C*D^n$ (Murray 1926, Uylings 1977) is confirmed, where n is fitted and plotted as well in Figure 38. These fits have R^2 correlation values greater than 0.75, as listed in Table 5 for each group. The individual branch values of n are plotted as probability distribution functions in Figure 39. While the stable COPD and normal smoker cases have well defined peaks at approximately 2.5, the decliner COPD case has a smaller but still well-defined peak around 3, and the decliner COPD 5 year has no well-defined peak, but rather a large plateau between 3 and 4. The significant variations in n between subject cases is significant when compared to the diameter exponent m described in section 3.1.1, for the m results showed little to no variation between subject groups.

Just as h_{min} relates the minor child to parent diameters, the flow diving ratio r is the ratio of the minor child branch flow rate to the parent branch flow rate. The mean values over all branches are listed in Table 5. All four subject groups are of similar values

between 0.27 and 0.34. This further validates the trend that the minor branch sibling typically has a smaller flow rate than its major sibling. The generational progression of r is shown in Figure 40, which confirms that all four subject cases behave the same way.

Case	Flow dividing ratio r	Fitted n value	R^2 value of fitted n
Decliner COPD 5 year	0.31 ± 0.14	3.56	0.76
Decliner COPD	0.27 ± 0.14	2.59	0.77
Stable COPD	0.34 ± 0.15	2.78	0.83
Normal smoker	0.32 ± 0.16	2.36	0.80

Table 5 Values of the flow dividing ratio r and the least squares fit of the flow rate vs. diameter exponent n for each subject. Also listed is the statistical robustness – R^2 – of the fitted n value.

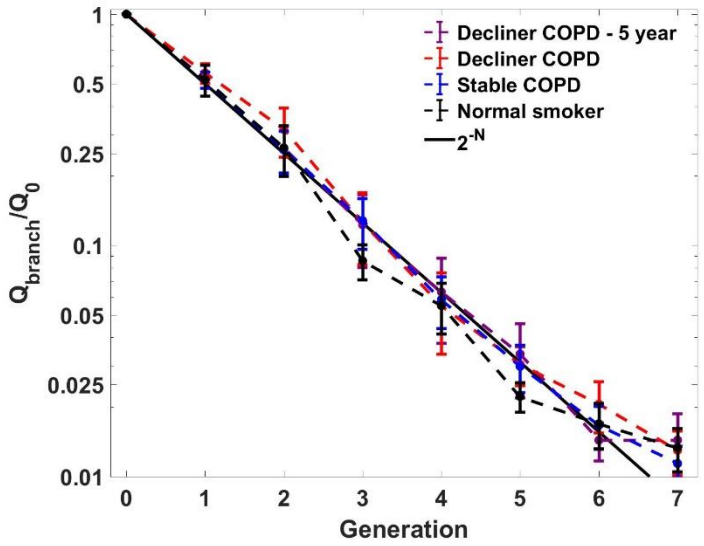

Fig. 37 Lin-log plot of branch flow rate vs. generation. Averages over each generation calculated for each subject. Also plotted is the theoretical branch flow rate in a dichotomous model. Error bars reported in standard error.

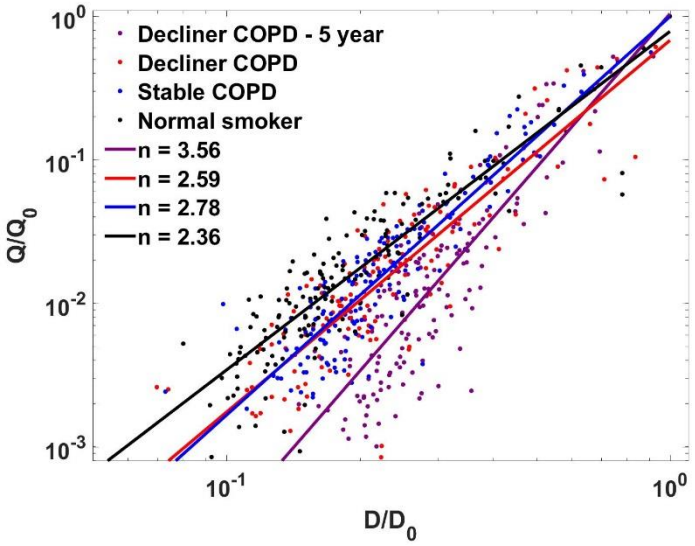

Fig. 38 Scatter of branch flow rate normalized by trachea flow rate vs. branch diameter normalized by trachea diameter for each subject. Also plotted is a least squares fit of the power law $Q = C*D^n$ for each subject.

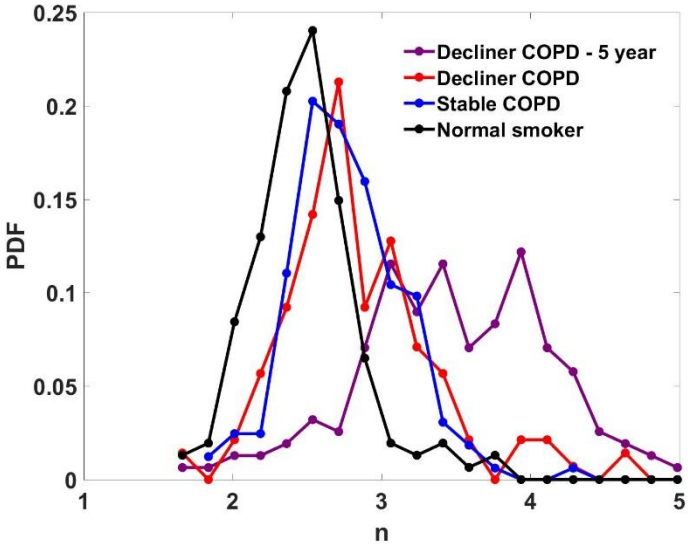

Fig. 39 Probability Distribution Function of the n exponent satisfying the power law $Q = C*D^n$ for each subject.

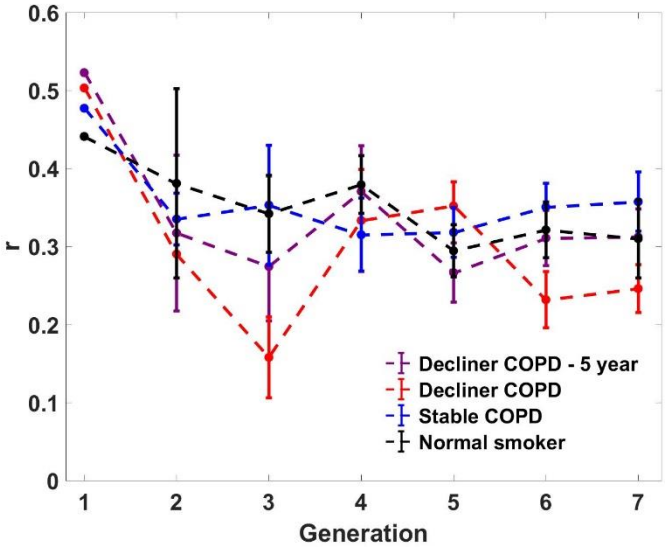

Fig. 40 Flow dividing ratio r vs. generation. Averages over each generation calculated for each subject. Error bars reported in standard error.

Chapter 4: Conclusions/Future Work

4.1 Summary

Morphological and experimental fluid mechanics analysis was performed on airway trees reconstructed from CT scans. 5 subject groups – decliner COPD at baseline, decliner COPD after 5 years of decline, stable COPD, normal smoker, and normal non-smoker – were explored for the morphological analysis. Through a centerline analysis algorithm, various geometrical parameters were calculated. Some of these, such as the homothety ratio h, were confirmed to have values of approximately 0.78, similar to previous findings. The ratio of sibling diameters, D_{min}/D_{maj}, and the branch angle, θ, were also found to match previous findings with an average value of 0.85 and 66°, respectively. On the other hand, the length to diameter ratio, L/D, was found to have non-monotonic behavior throughout the airway generations, increasing from about 1.5 at G2 and reaching approximately 4.5 by G7. This is in stark contrast with previous findings, which reported L/D as a constant throughout the airways. It was also found that the L_{min} is typically considerably larger than L_{maj}, and the sibling length ratio L_{min}/L_{maj} has a negative correlation with D_{min}/D_{maj}. The COPD subjects showed smaller airway lumen (when normalized by the trachea diameter), as expected. 3D fractal analysis of the airways reveals that the airways are self-similar with a fractal dimension typically around 1.85. Smoking as well as the onset of COPD appears to alter the airways such that the fractal dimension decreases. However, once severe COPD is attained, airways changes tend to bring the fractal dimensions back to levels shown by smokers with marginal airflow obstruction.

Using MRI velocimetry, 3D flow fields were acquired in 3D printed flow models built to replicate the subject-specific airway geometry. Imposing calculated lobar ventilation ratios as outlet conditions, steady flow inhalation was studied. Using the E parameter to quantify secondary flows, values were found to be in the range of previous 3D MRI velocimetry studies on the airways such as Banko et al. (2015) in subject-specific study, and significantly higher than in idealized (Weibel-type) geometries (see

Jalal et al. 2016). Through branch and generational analysis, secondary flows were found to be significantly stronger in decliner COPD subjects than the in normal smoker and stable COPD subjects. In general, the results support the assumption that airway structure and the consequent respiratory flow features correlate with the status and progression of the disease.

4.2 Future Work

This study represents the first step in the investigation of respiratory flows in our research group, and future work is warranted to overcome its present limitations. While the COPDGene study has enrolled over 10,000 subjects, this study has reconstructed and analyzed the structure of only 90 subjects. Studying a much larger cohort of the COPDGene subject would improve the statistical power of the results, and may lead to more significant findings. Additionally, airways were only successfully reconstructed up to the 7th generation in most subject cases. Due to their unhealthy release of radiation into the human body, CT scans are kept at low radiation dosage and can only provide limited resolution of the human airways. Ex-vivo CT scans of lungs have been performed using higher radiation doses – which in turn results in much higher scan resolution – but ex vivo lungs may be deformed and improperly inflated, giving inaccurate results. The use of high resolution MRI scans to obtain the airway geometry would likely provide analysis into the deeper airways, the ones in which particle deposition is thought to be more harmful.

The flow experiments conducted on the models also have obvious limitations. While the outlet flow rates were imposed on a lobar level, the model has distal airways of varying diameter and generation depth. This likely leads to imbalance of airflow through the various airways within each lobe, because the outlet pressure imposed to each terminal branch is effectively the same. While imposing a flow rate boundary condition at each terminal branch would be of high difficulty in an experimental setting, determining the specific boundary condition at each branch is of greater difficulty. It remains unknown whether it is most appropriate to impose a branch-specific outlet flow rate or a

branch specific outlet pressure. The inlet of the flow models in this experiment did not exactly match known tracheal inlet flow conditions. Other studies, such as Banko et al. (2015) reconstructed the trachea and mouth fully, connecting their flow loop system to the subject's reconstructed mouth. This successfully recreated the epiglottal and laryngeal jets that this study did not. In their CFD study, Choi and Lin (2010) apply the full breathing cycle of inhalation and exhalation to their model. While this study was focused on the inhalation cycle, future work into the full breathing cycle similar to Choi and Lin would likely provide valuable insight into particle deposition and flow mixing in the airways. Additionally, while this study's models were rigid, the airways are deformable and their geometry changes throughout the breathing cycle. Miyawaki et al. (2016) created a time-varying CT reconstructed model of the airways throughout the breathing cycle. Creating a non-rigid experimental model with similar material properties to the airways would allow exploration into the geometry and air flow relationship through the totality of the breathing cycle. This, however, would require knowledge of the airway tissue compliance, which is only known indirectly from pressure-volume correlation, and may vary significantly with further generations. Therefore, while future studies on fluid-structure interaction are warranted, they will likely require advanced manufacturing with materials of prescribed spatial variation of elasticity. Recent and fast-paced developments in 3D printing provide exciting perspectives in this direction.

Bibliography

Antonelli-Incalzi R, Imperiale C, Bellia V, et al. Do GOLD stages of COPD severity really correspond to differences in health status? Eur Respir J 2003; 22:444–9.

Banko AJ et al. Three-dimensional inspiratory flow in the upper and central human airways. Exp Fluids 2015; 56(6):1–12

Banko, A. J., Coletti, F., Elkins, C. J., & Eaton, J. K. Oscillatory flow in the human airways from the mouth through several bronchial generations. International Journal of Heat and Fluid Flow 2016; 61:45-57.

Campbell R. Describing the shapes of fern leaves: A fractal geometrical approach. Acta Biotheoretica 1996; 44:119-142.

Celli BR, MacNee W, Agusti A, et al. Standards for the diagnosis and treatment of subjects with COPD: a summary of the ATS/ ERS position paper. Eur Respir J 2004; 23:932–46

Yin Y, Choi J, Hoffman EA, Tawhai MH, Lin CL. Simulation of pulmonary air flow with a subject-specific boundary condition. Journal of biomechanics. 2010 Aug 10;43(11):2159-63.

Choi J, Xia G, Tawhai MH, Hoffman EA, Lin CL. Numerical study of high-frequency oscillatory air flow and convective mixing in a CT-based human airway model. Annals of biomedical engineering. 2010 Dec 1;38(12):3550-71.

De Backer JW et al. Flow analyses in the lower airways: subject-specific model and boundary conditions. Medical engineering & physics 2008; 30(7):872-879

De Backer W et al. Lung deposition of BDP formoterol HFA pMDI in healthy volunteers, asthmatic, and COPD subjects. Journal of aerosol medicine and pulmonary drug delivery, 2010; 23(3):137-148

Elkins CJ et al. Magnetic resonance velocimetry: applications of magnetic resonance imaging in the measurement of fluid motion. Experiments in Fluids 2007; 43(6):823-858.

Fletcher C, Peto R. The natural history of chronic airflow obstruction. British medical journal. 1977;1(6077):1645-1648

Fresconi, F. E., & Prasad, A. K. Secondary velocity fields in the conducting airways of the human lung. Journal of biomechanical engineering 2007; 129(5), 722-732.

Glenny RW & Robertson HT. Determinants of pulmonary blood flow distribution. Comprehensive physiology 2007.

Goldberger AL & West BJ. Chaos and order in the human body. MD computing: computers in medical practice 1991; 9(1):25-34.

Grotberg JB. Pulmonary flow and transport phenomena. Annual Review of Fluid Mechanics 1994; 26(1):529-571

Hausdorff F. Dimension und äußeres Maß. Mathematische Annalen. 1918 Mar 1;79(1):157-79.

Horsfield K & Cumming G. Morphology of the bronchial tree in man. Journal of Applied Physiology 168; 24(3):373-383

Horsfield K, Dart G, Olson DE, Filley GF, Cumming G. Models of the human bronchial tree. Journal of applied physiology. 1971 Aug 1;31(2):207-17.

Isabey D & Chang HK. A model study of flow dynamics in human central airways. Part II: Secondary flow velocities. Respiration physiology 1982; 49(1):97-113

Jalal S et al. Three-dimensional inspiratory flow in a double bifurcation airway model. Experiments in Fluids 2016; 57(9):148

Kleinstreuer C & Zhang Z. Airflow and particle transport in the human respiratory system. Annual Review of Fluid Mechanics 2010; 42:301-334

Mandelbrot BB. The Fractal Geometry of Nature. WH Freeman and Co 1983.

Mandelbrot, B. Fractals-a geometry of nature. New Scientist 1990; 127(1734), 38-43

Markl M et al. 4D flow MRI. Journal of Magnetic Resonance Imaging 2012; 36(5):1015-1036.

Masters, B. R. Fractal analysis of the vascular tree in the human retina. Annu. Rev. Biomed. Eng. 2004; 6, 427-452.

Minino AM, Xu J, Kochanek KD. Deaths: preliminary data for 2008. National vital statistics reports: from the Centers for Disease Control and Prevention, National Center for Health Statistics, National Vital Statistics System. 2010; 59(2):1-52.

Miyawaki, S., Hoffman, E. A., & Lin, C. L. Effect of static vs. dynamic imaging on particle transport in CT-based numerical models of human central airways. Journal of Aerosol Science 2016; 100, 129-139.

Murray CD. The physiological principle of minimum work I. The vascular system and the cost of blood volume. Proceedings of the National Academy of Sciences 1926; 12(3):207-214.

Padilla A. The effect of upstream perturbations on 3D annular diffusers. PhD thesis, Stanford University 2012.

Pedley TJ. Pulmonary fluid dynamics. Annu Rev Fluid Mech 1977 9(1):229–274

Phillips CG & Kaye SR. Diameter-based analysis of the branching geometry of four mammalian bronchial trees. Respiration physiology 1995; 102(2-3):303-316.

Rabe KF, Hurd S, Anzueto A, et al. Global strategy for the diagnosis, management, and prevention of chronic obstructive pulmonary disease: GOLD executive summary. Am J Respir Crit Care Med 2007;176:532–55

Regan EA et al. Genetic epidemiology of COPD (COPDGene) study design. COPD: Journal of Chronic Obstructive Pulmonary Disease 2011; 7(1):32-43.

Sapoval B, Filoche M, Weibel ER. Smaller is better—but not too small: a physical scale for the design of the mammalian pulmonary acinus. Proceedings of the National Academy of Sciences. 2002 Aug 6;99(16):10411-6.

Sauret V et al. Study of the three-dimensional geometry of the central conducting airways in man using computed tomographic (CT) images. Journal of anatomy 2002; 200(2):123-134.

Tawhai MH et al. CT-based geometry analysis and finite element models of the human and ovine bronchial tree. Journal of applied physiology 2004; 97(6):2310-2321.

Uylings HBM. Optimization of diameters and bifurcation angles in lung and vascular tree structures. Bulletin of mathematical biology 1977; 39(5):509-520.

Weibel ER. Principles and methods for the morphometric study of the lung and other organs. Lab Investig J Tech Methods Pathol 1963; 12:131

Weibel ER. What makes a good lung. Swiss Med Wkly 2009; 139(27-28):375-386.

West GB et al. A general model for the origin of allometric scaling laws in biology. Science 1997; 276(5309):122-126.

Wilson TA. Design of the bronchial tree. Nature 18 1969; 668–669.